Planetary and Space Science 180 (2020) 104764

Contents lists available at ScienceDirect

Planetary and Space Science

journal homepage: www.elsevier.com/locate/pss

Digital terrain mapping by the OSIRIS-REx mission

O.S. Barnouin [a,*], M.G. Daly [b], E.E. Palmer [c], C.L. Johnson [c,d], R.W. Gaskell [c], M. Al Asad [d], E.B. Bierhaus [e], K.L. Craft [a], C.M. Ernst [a], R.C. Espiritu [a], H. Nair [a], G.A. Neumann [f], L. Nguyen [a], M.C. Nolan [g], E. Mazarico [f], M.E. Perry [a], L.C. Philpott [d], J.H. Roberts [a], R.J. Steele [a], J. Seabrook [b], H.C.M. Susorney [d], J.R. Weirich [c], D.S. Lauretta [g]

[a] The Johns Hopkins University Applied Physics Laboratory, 11100 Johns Hopkins Rd, Laurel, MD, 20723-6099, USA
[b] The Centre for Research in Earth and Space Science, York University, Toronto, Ontario, M3J 1P3, Canada
[c] Planetary Science Institute, 1700 East Fort Lowell, Suite 106, Tucson, AZ, 85719-2395, USA
[d] Department of Earth, Ocean and Atmospheric Sciences, University of British Columbia, Vancouver, BC V6T 1Z4, Canada
[e] Lockheed Martin Space Systems Company, PO Box 179, Mail Stop S8110, Denver, CO, 80201, USA
[f] NASA Goddard Space Flight Center, Greenbelt, MD, USA
[g] Lunar and Planetary Laboratory, University of Arizona, Tucson, AZ, USA

ARTICLE INFO

Keywords:
Asteroid shapes
Digital terrain models
Stereophotoclinometry
Laser altimetry
(101955) bennu
OSIRIS-REx mission

ABSTRACT

The Origins, Spectral Interpretation, Resource Identification, Security–Regolith Explorer mission will return a sample to Earth from asteroid (101955) Bennu. Digital terrain models (DTMs) of the asteroid, and products enabled by them, are key to understanding the origin and evolution of the asteroid, providing geological and geophysical context for the sample, maximizing the amount of sample returned, navigating the spacecraft, and ensuring the safety of the spacecraft during sampling.

The mission has two approaches for producing these DTMs: a camera-based approach and a lidar-based approach. We provide an overview of the methods used for these two approaches and how they fit into the originally planned mission. We also discuss a summary of tests using these plans to evaluate the expected performance of the DTMs and describe the data products derived from them.

1. Introduction

The Origins, Spectral Interpretation, Resource Identification, Security–Regolith Explorer (OSIRIS-REx; Lauretta et al., 2017) mission will sample asteroid (101955) Bennu (hereafter, Bennu; Lauretta et al., 2015). The mission's Altimetry Working Group (AltWG) is responsible for generating all of the global and local digital terrain models (DTMs) of Bennu (Fig. 1). The AltWG also produces a suite of surface tilt maps and geodetic products (e.g., slope, gravity) that use the mass of the asteroid determined via radio science (two-way tracking) to estimate a gravitational potential field or geoid (Scheeres et al., 2016). The geoid is necessary to produce digital geopotential altitude or elevation maps that measure topography as defined on other planets. The AltWG additionally produces 1064-nm reflectance maps using the OSIRIS-REx Laser Altimeter (OLA, contributed by the Canadian Space Agency; Daly et al., 2017) and relative albedo maps using the OSIRIS-REx Camera Suite (OCAMS; Rizk et al., 2018).

The altimetry products are critical for the science activities and sampling efforts of the OSIRIS-REx mission. At a global scale, DTMs are vital to inferring the geological origin and evolution of the asteroid by, for example, constraining its bulk density through precise volume measurement and the mass estimate yielded from radio science (Scheeres et al., 2016). The bulk density provides clues to the nature of the porosity within Bennu, which in turn constrains the asteroid's origin and collisional evolution (e.g., Yeomans et al., 1997, 1999; Wilkison et al., 2002; Abe et al., 2006; Campins et al., 2010; Chesley et al., 2014; Walsh and Lauretta, 2013; Bottke et al., 2015). The global maps of slopes, geopotential elevation, and surface roughness provide quantitative data that give additional insights into surface processes that influence the evolution of the regolith (e.g., Cheng et al., 2001, 2002; Miyamoto et al., 2007; Barnouin-Jha et al., 2008; Scheeres et al., 2016). The global DTMs are also necessary to assess whether surface lineaments have measurable topography, and they provide the context for determining the relationship of these lineaments to any other surface features (such as craters or

* Corresponding author.
E-mail address: olivier.barnouin@jhuapl.edu (O.S. Barnouin).

https://doi.org/10.1016/j.pss.2019.104764
Received 22 October 2018; Received in revised form 15 August 2019; Accepted 4 October 2019
Available online 12 October 2019

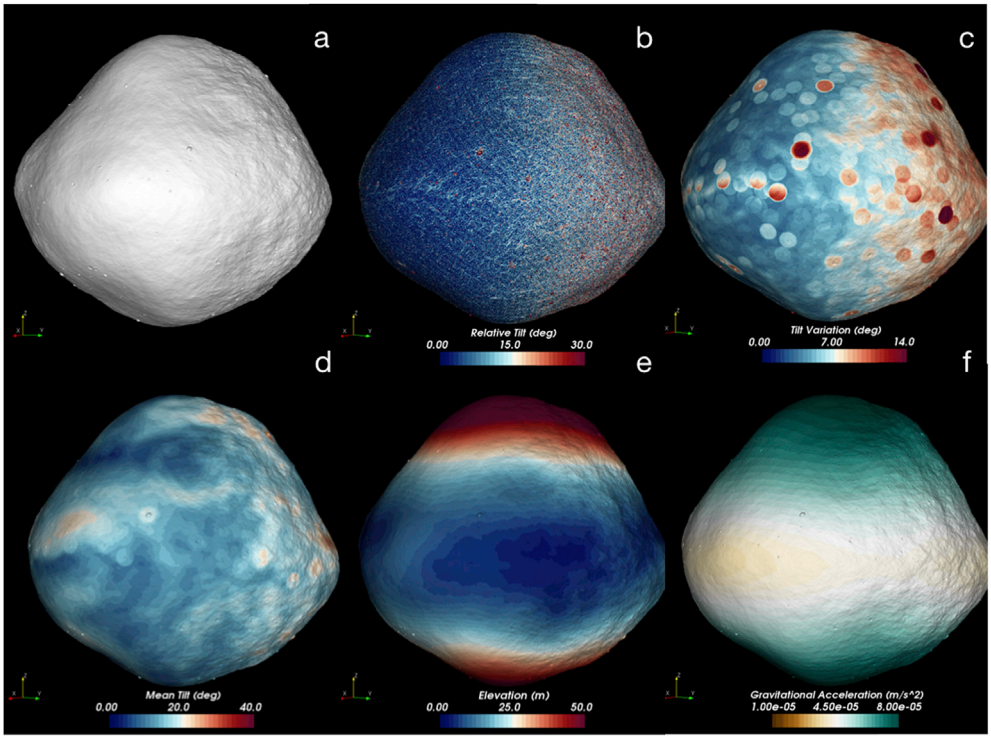

Fig. 1. Simulated examples of global products produced from SPC or OLA data. The shape model (a) comes with information on surface tilts (b through d) necessary for ensuring safe sampling and assessing surface sampleability. Geodetic products such as geopotential elevation (e) and gravitational acceleration (f) allow evaluation of the surface processes that are modifying Bennu.

boulders) of the asteroid. These types of lineament assessments can help constrain the internal nature of asteroids, including Bennu (e.g., Buczkowski et al., 2008; Jaumann et al., 2012; Besse et al., 2014; Marchi et al., 2015; Tonge et al., 2016). Furthermore, the global shape models and maps of surface tilt and vertical roughness provide critical early products for identifying potential sample sites with minimal surface hazards.

At the predicted sample-site scale (<25 m in diameter), the DTM products provide detailed information on the geological and geophysical surface processes that influence the regolith for surface extents similar in size to the OSIRIS-REx sampling device (0.32 m radius; Bos et al., 2018; Bierhaus et al., 2018). The sample-site products of geopotential slope, geometric tilt distributions, and geometric heights of any boulders within the sample ellipse play an essential role in understanding the geology at the sample site (e.g, Miyamoto et al., 2007; Murdoch et al., 2015; Thomas and Robinson, 2005; Yu et al., 2014; Rubincam, 2000; Walsh et al., 2008; Scheeres et al., 2016) and ensuring that hazards are kept to a minimum while maximizing the performance of the OSIRIS-REx sampling system—thereby enabling the collection of a larger mass of sample.

In addition to supporting these scientific needs, the DTM products also aid spacecraft navigation. The OSIRIS-REx mission has performed optical navigation throughout proximity operations (Jackman et al., 2017; Williams et al., 2018) and will use natural feature tracking (NFT), an autonomous navigation approach, during the final approach for sample collection (Mario and Debrunner, 2016; Lauretta et al., 2017; Williams et al., 2018). Both navigation efforts require high-accuracy maps for landmark navigation (MLNs), which include surface heights in the form of a DTM and associated albedo data. During the early mission phases, the spacecraft collects the data needed to generate the MLNs required by the Flight Dynamics System team (FDS) for the later phases. These early-mission data include imaging and laser altimeter measurements obtained during an Approach imaging campaign and several hyperbolic flybys (Lauretta et al., 2017; Daly et al., 2017). The higher-resolution data needed for NFT are collected later during two orbital phases, a Detailed Survey phase, and several sample-site reconnaissance passes.

In this paper, we review the observations designed by the OSIRIS-REx mission in support of the development of DTMs and related products. We demonstrate how these observations satisfy the needs to produce image- and altimeter-derived global and local DTMs and MLNs and discuss the testing that we used to predict their expected quality following the various mission phases. Also, we define and provide examples of ancillary products necessary to safely sample Bennu, such as maps of geometric surface tilt and geopotential slope.

2. Observations

We derive DTM products from two separate sets of OSIRIS-REx observations of Bennu. The first set is obtained with OCAMS (mainly the PolyCam and MapCam cameras; Rizk et al., 2018) in support of the shape model construction technique called stereophotoclinometry (SPC; Gaskell et al., 1988). PolyCam is a narrow-field, 630-mm-focal-length (at ∞ range) f/3.5 Ritchey-Chretien telescope with a 13.8 mrad field of view (FOV) and a 0.0135 mrad instantaneous field of view (IFOV). MapCam is a medium-field imager, with a 125-mm-focal-length f/3.3 optical system that provides a ~70 mrad FOV and a IFOV of 0.068 mrad. OLA acquires the second set of observations. OLA is a laser altimeter with a scanning mirror capable of measuring ranges over a 10° by 10° field of regard, with individual footprint of either 100 or 200 μrad, fired at 0.1 or 10 kHz. OLA provides a self-consistent set of laser return locations in 3D, henceforth called point clouds, that can be tiled together to produce global and local surface DTMs. The OCAMS and OLA data sets are used independently to generate separate DTMs and associated products. This independence provides a way to verify the products.

The OCAMS and OLA observation sets each enable the generation of complete global DTMs with a ground sample distance (GSD) of ~0.75 m and an estimated absolute spatial accuracy of <0.5 m. They also provide the data needed to generate a complete global set of higher-resolution DTMs that tile the entire asteroid with GSDs of approximately 0.32 and

0.08 m. Although OLA data are the primary source for the sample-site DTMs with GSDs of ≤0.05 m, in the best-case scenarios, we can use both sets of observations to generate these products. Furthermore, the two data sets support independent estimation of the asteroid's pole position and rotation rate and the identification of the center-of-mass center-of-figure offset. The OLA and OCAMS data also support NFT by providing up to 300 MLNs, some of which require a GSD of 0.08 m.

2.1. OCAMS imaging

The critical periods of the mission in which OCAMS observations were designed to support SPC shape modeling include the Approach, Preliminary Survey, Orbital A, and Detailed Survey mission phases (Fig. 2; Table 1). Approach data needed to generate a global DTM with a GSD of 0.75 m via SPC are acquired when Bennu is at least 100 pixels across in the PolyCam FOV. This condition occurs at a range of <160 km from Bennu. Initially, the range to Bennu is sufficiently large that a single nadir-point PolyCam frame can image Bennu within navigational uncertainties. Four or more rotations of Bennu are acquired, with one image taken at every 10° of rotation. The multiple rotations provide an arc of time long enough to assess the asteroid's obliquity and rotation rate. Later, as Bennu fills a more substantial fraction of the FOV, four additional rotation sequences are acquired, each captured every 10°–20° of rotation in a suite of mosaics 4 × 4 or larger. The GSD per pixel of these images ranges from 2 to 0.3 m. SPC requires four images in each of the cardinal directions (E, W, N, S) and one image at low phase, with appropriate variations in the Sun angle and GSDs (see Secion 3.1 for additional details). The SPC coverage that was expected for the Approach phase is shown in Fig. 3 and illustrates that this phase of the mission partially satisfies SPC needs for modeling the equator, but does not provide any useful data for the poles, apart from some limb information.

Polar imaging coverage needed by SPC for the generation of the global DTM is obtained from Preliminary Survey MapCam images. These images provide resolutions similar to those obtained during Approach with PolyCam, but with a different set of look angles (defined as angles to the nominal Bennu surface normal and usually separated by 20° or more of stereoscopic parallax) that enhance stereo information. Such stereo data greatly aid the production of the global DTM. The images are acquired on three flybys, over the north pole, the equator, and the south pole of Bennu during their inbound and outbound portions. MapCam image mosaics that are either 2 × 2 or 2 × 5 in size accommodate navigation errors for every 10° of asteroid rotation, with image GSDs ranging from 0.75 to 0.55 m.

Based on our extensive testing (see Section 3.1), the addition of the imaging data from Preliminary Survey to that from the Approach phase satisfies the SPC requirements for making the global DTM with a GSD of 0.75 m (Fig. 3). The one albedo image and the four cardinal-direction images needed for shape modeling with SPC are obtained for more than 80% of the asteroid, with GSDs ranging from 3.0 to 0.3 m. The lack of data near the poles is mitigated to some extent by the presence of limbs that help constrain the shape of the asteroid in those regions.

Images from the subsequent observation phases inform the generation of the highest-resolution DTMs produced with SPC. These include a set of local DTMs with GSDs of 0.32 m, which, tiled together, produce a global product, and 300 local NFT MLNs with GSDs of 0.08 m.

The subsequent observation phases begin with an initial set of MapCam images, specifically of latitudes ±(55°–70°), obtained in the last few days of Orbital A and providing a set of down-looking views of the poles. These images have a GSD of 0.07 m. Then, a set of MapCam and PolyCam data with GSDs of 0.25 m are acquired in Detailed Survey, during several equatorial stations in which the asteroid is observed at different times of day. These data provide near-nadir views of the surface at varying Sun angles and cover either one or two of the four cardinal directions around the equator needed by SPC to produce high quality DTMs with GSDs of 0.32 and 0.08 m. Finally, up to seven N–S flybys near 3.5 km acquire PolyCam images with GSDs of 0.05 m at different times of day, providing the remaining cardinal E– and W-look directions needed to generate SPC DTMs with GSDs of 0.32 m. Our testing indicates that extrapolation of the imaging data may permit the generation of sample-site DTMs with GSDs near 0.05 m using SPC, despite not fulfilling all of SPC's imaging requirements. However, these latter products, along with the SPC estimates of relative albedo, are useful in MLNs for navigation and for NFT to identify landmarks and triangulate, but do not alone supply sufficiently high-fidelity geometric surface height data for spacecraft safety and sampling needs. These high-fidelity geometric height data come later, from OLA (see Section 2.2).

The later mission phases do not have any specific SPC objectives, but all the images acquired in Orbital B and the Reconnaissance (Recon) phase are expected to enhance SPC-derived DTMs and ultimately make their way to the final SPC product delivered to the NASA Planetary Data System. Testing shows that even if the images do not have ideal SPC viewing geometries, the improved resolution of images provides better-resolved tilts and surface heights in any SPC-derived DTMs.

2.2. OLA observations

OLA observations have two main objectives. In the early phases of the mission, when the OSIRIS-REx spacecraft is relatively far from Bennu (~7 km), OLA provides early verification of the asteroid scale produced by SPC and an independent means to assess spacecraft navigation

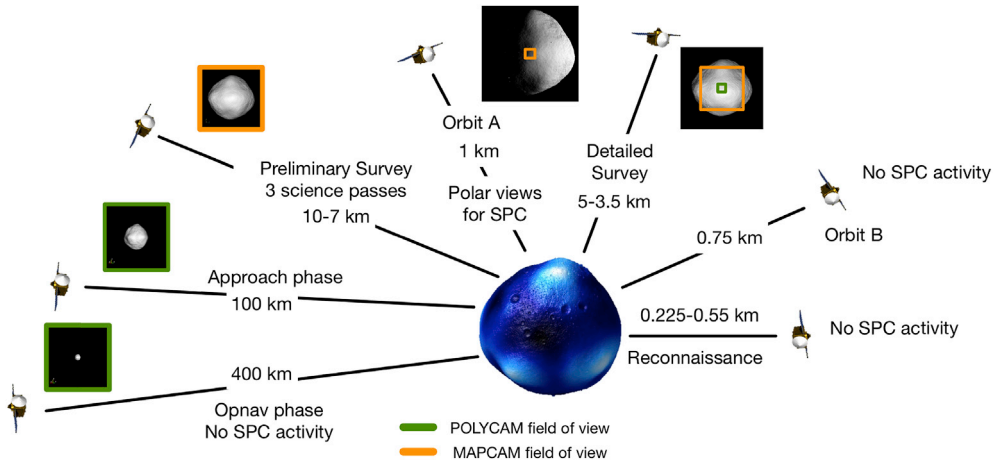

Fig. 2. OCAMS observations designed in support of SPC. Mission phases are shown in chronological order (clockwise; see Table 1 for more details; Lauretta et al., 2017).

Table 1
OCAMS and OLA observations designs (Figs. 2 and 6) used in presented tests.

Mission Phase	Range to asteroid (km)	Imaging GSD		OLA scan pattern, scan size, footprint diameter, collection rate			
		PolyCam (m/pix)	MapCam (m/pix)	Scan Pattern	Scan Size (deg)	Footprint Diameter (m)	Rate (kHz)
OpNav	400	5.4	NA	NA			
Approach	100	1.4	NA	NA			
Preliminary Survey	10–7	0.35–0.1	0.7–0.5	Linear	±5	2–1.4	0.1
Detailed Survey	5–3.5	0.07–0.05	0.4–0.24	Linear	±0.23	1–0.7	0.1
Orbital B	0.75	0.01	0.05	2D raster	±6	0.075	10
Reconaissance	0.55–0.0225	0.01–0.003	0.04–0.017	Linear	±0.23	0.055–0.0225	10

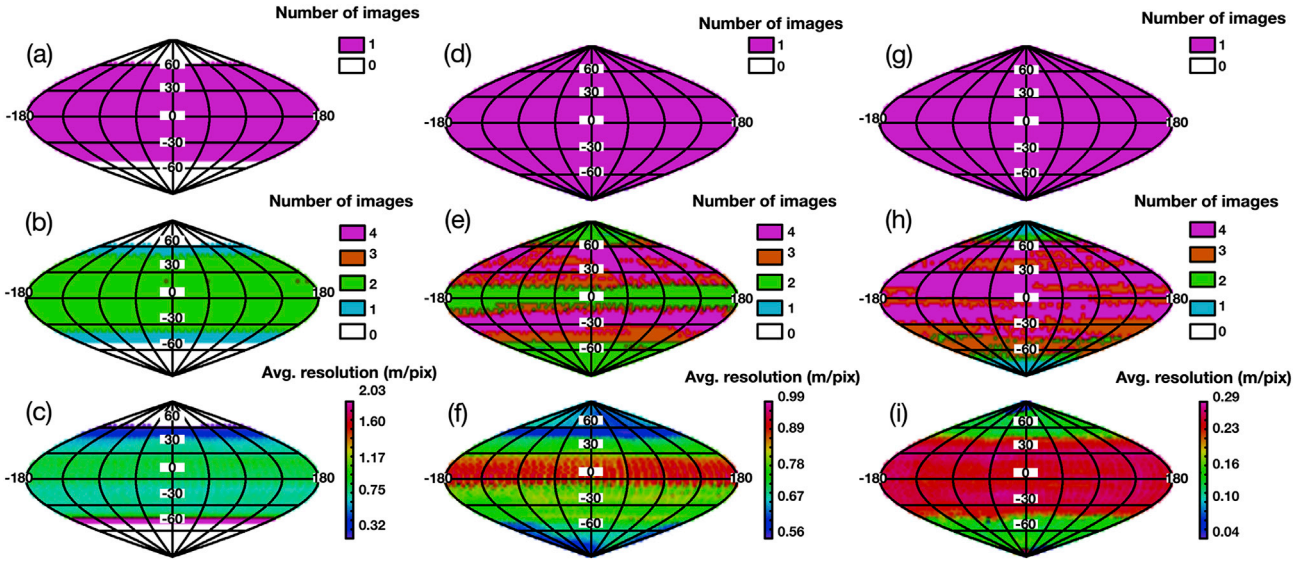

Fig. 3. OCAMS image coverage for SPC, expressed as the number of images covering an area, designed for Approach (a–c), Preliminary Survey (d–f), and Detailed Survey (g–i). The observation design satisfies the requirements for SPC imaging to generate the 0.75-m global DTM after Preliminary Survey and the 0.35-m (or better) global DTM after Detailed Survey for regions below 70° latitude. The results show that the mission collects at least one albedo image (a, d, g) with low Sun angles (<10°), at least four cardinal-direction images (b, e, h), and images with GSDs between 0.3 and 1 m (c, f, i). Only the poles have limited coverage, but these regions make up less than 20% of the surface area of the asteroid.

solutions. Later, OLA's scanning capability dramatically reduces the mission timeline by making very high-resolution DTMs with GSDs of 0.08 m globally and <0.05 m locally for sample sites.

The early OLA measurements are critical to quickly address any camera issues or biases that might have occurred in the SPC and navigation process. Although typically minor, experience shows that uncertainties in a camera's focal length or distortions can sometimes lead to problems in the results of SPC shape modeling. Furthermore, uncertainties in spacecraft pointing and range to a target can lead to degeneracy in the SPC solution, where the spacecraft pointing and range estimated by SPC cannot be easily deconvolved. This situation can result in uncertainties in the overall scale of any modeled asteroid. The problem can be mitigated using a variety of techniques, including making use of radio science tracking data to derive the spacecraft velocity upon approach to the asteroid with appropriate imaging. However, by far the most time-efficient technique is to identify issues using direct range measurements to the surface from OLA, especially early in the mission, so that any adjustment to the scale of topographic products can be made promptly, with minimal impact downstream on the rest of the products. Such laser altimeter data was invaluable for correctly modeling the scale of 25143 Itokawa with the images from the JAXA Hayabusa mission (Gaskell et al., 2008). Spacecraft navigation also benefits from such range data because they provide an additional absolute-scale measurement that helps better identify small forces acting on the spacecraft resulting from either solar thermal radiation impinging on the spacecraft or slow outgassing of the spacecraft. These forces are sometimes difficult to model accurately but substantially influence trajectory estimates when a spacecraft is moving slowly relative to its target, as is the case for OSIRIS-REx.

The OLA operations that acquire measurements within 1 km from the surface are relatively simple because of the operational flexibility of the OLA scanning mirror (Daly et al., 2017). At this distance, an individual OLA raster scan (typically 100 m × 100 m) can provide an accurate DTM of the surface of Bennu (Fig. 4). A combination of a few of these scans, or just one scan acquired during a close-up flyby near 225 m, provides a DTM of a prospective sample site with the required GSD of 0.05 cm. A global set of the scans collected from 1-km orbit helps satisfy the sampleability, safety, and NFT interest in having a global set of DTMs with GSDs of 0.08 m. Simulations show that OLA collects a set of scans within one month of orbit operations at 750-m range to make this high-resolution 0.08-m global DTM, where each 0.08-m bin of the global DTM frequently contains more than five returns (Fig. 5). Having many such returns minimizes the vertical uncertainties associated with the DTM. Such products can be obtained for more than 80% of the asteroid's surface area even when considering some reasonably large spacecraft excursions (up to several hundreds of meters along-track). Likewise, just one flyby of a proposed sample site near 225 m acquires a DTM with a GSD of 0.03 m, with an equally large number of returns in each 0.025-m bin. Using SPC to make a similar set of global and local DTMs at the fidelity needed for spacecraft safety and sampling requires a much more complicated set of observations near the asteroid, because of the resolution and cardinal viewing direction needed by SPC. Implementing these would result in a complicated imaging plan that would strain the mission's human resources, cost, and schedule.

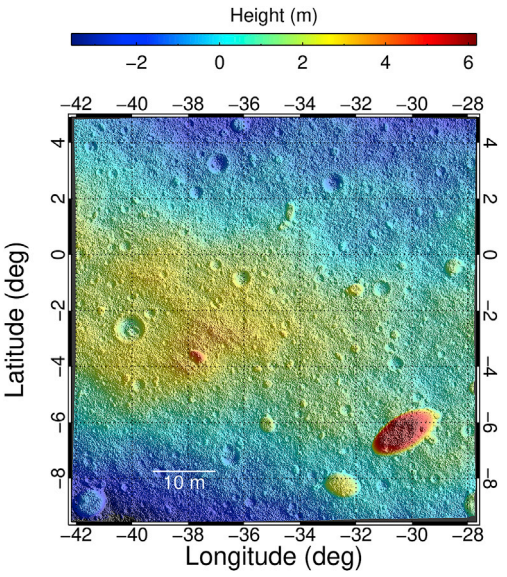

Fig. 4. Sample simulated DTM produced by one OLA scan from a range of ~750 m. The salt and pepper texture is due to the enhanced noise of ±0.03 m added to the OLA ranges in this simulation. Lab data indicate actual range accuracies associated with individual OLA data are ±0.01 m (Daly et al., 2017).

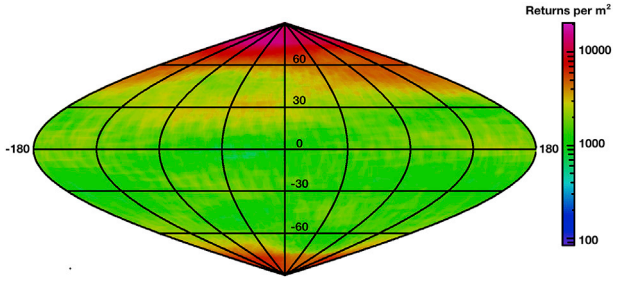

Fig. 5. Expected spatial density of OLA returns with emission angles less than 45° during Orbital B from ~750 m. This coverage provides more than five returns in each bin of the global 0.08-m DTM. In particular, expected OLA data fill the polar regions that are less well covered by SPC.

The OLA observations (Fig. 6) begin with a set of long-range observations at Preliminary Survey near 7 km from the asteroid. Here, OLA scans perpendicular to the direction of the spacecraft trajectory for ~75 min, once just before closest approach and once just after. In this phase, OLA uses its High Energy Laser Transmitter (HELT), capable of ranging at 100 Hz to a surface <10 km away, and the laser beam divergence results in footprint sizes of ~2.0 m. These observations are undertaken during four of the five Preliminary Survey flybys, with two passes over the north pole and one each over the south pole and equator. The next set of OLA observations occurs during the Detailed Survey. Again using the HELT, OLA scans perpendicular to the N–S slews undertaken by the spacecraft to measure ranges to the surface with footprint sizes ranging from 0.35 to 0.7 m. The scans are obtained at five equatorial stations and four high-latitude stations—two near 40° latitude and two near −40° latitude. This diversity gives the first global coverage by OLA and makes it possible to build a 0.75-m shape model equivalent to the one developed using SPC after Preliminary Survey.

The next two sets of OLA observations occur in Orbital B and Recon and make use of the Low Energy Laser Transmitter (LELT). The LELT is used to range at less than 1000 m from the surface at 10 kHz. For Orbital B, the OLA footprints measure ~0.08 m. OLA collects a suite of individual 5.5 min long raster scans over a 10° x 10° field of regard separated by ~17 min, for two and half days after each optical navigation update. This generates a spiral of overlapping OLA raster scans around Bennu (Fig. 7). OLA maps the entire asteroid within 30 days. During Recon passes at 500 and 225 m from the surface, OLA undertakes a linear scan in the same direction as the spacecraft ground-track, making use of the spacecraft trajectory and slews, as it flies over potential sample sites.

3. Digital terrain model development

As discussed in Section 2, we use two approaches to construct the shape of Bennu. The first uses SPC with images collected by OCAMS. The second uses data collected by OLA. The two approaches are used separately to generate two independent products during flight that can be compared. They will ultimately be combined to exploit the strengths of each technique.

3.1. Stereophotoclinometry

The SPC implementation that we use was first developed in the mid-1980s to model the surface of Io (Gaskell et al., 1988). The implementation uses images obtained over a broad range of Sun (incidence) and observer (emission) angles to generate terrain and shape models of satellites, asteroids, planets, and comets. SPC has been used to model a broad suite of objects including but not limited to Phobos, Phoebe, Mars, Mercury, the Moon, 4 Vesta, 25143 Itokawa, and 67P/Churyumov–Gerasimenko (Fig. 8). SPC was initially developed as an optical navigation tool for spacecraft to identify specific landmarks or control

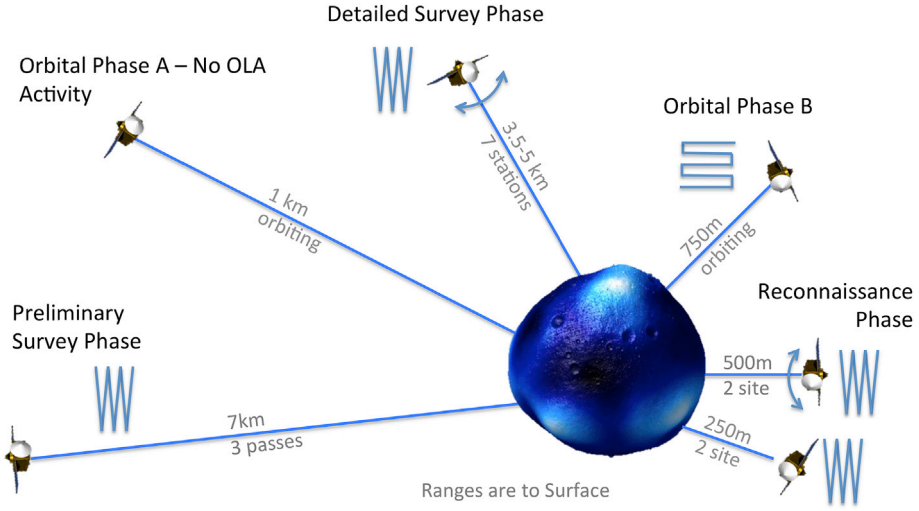

Fig. 6. OLA observations designed to support AltWG products (see Table 1 for more details).

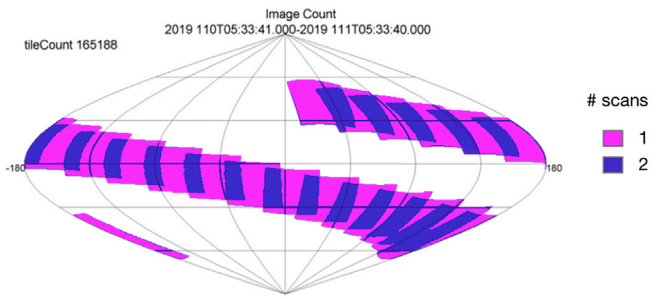

Fig. 7. The OLA observation design for Orbital B results in a series of overlapping raster scans that eventually cover the entire asteroid.

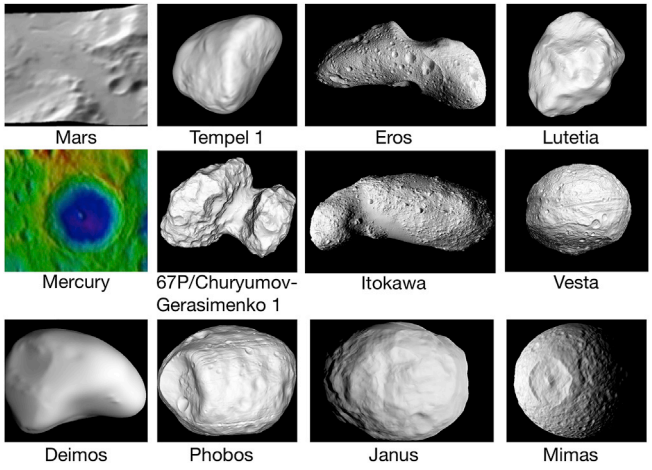

Fig. 8. Examples of past SPC models of planetary surfaces, comets, asteroids, and satellites.

points found on the surface of an asteroid or a planet under nearly any illumination and observation conditions (Gaskell et al., 2008). With these landmark positions, triangulation provides estimates of spacecraft trajectory and pointing in the reference frame of the observed body. For this navigation approach to work, the shape and relative albedo of the surface observed by the spacecraft needs to be well-modeled. SPC generates this model by combining geometric stereo techniques (e.g., Wolf and Dewitt, 2000) with photoclinometry, using both shading and lighting direction. SPC has been used successfully during operations to aid navigation at 25143 Itokowa, 4 Vesta, and 1 Ceres.

SPC makes use of all the images available, regardless of resolution. It builds initial models and provides an estimate of the asteroid's pole position and rotation rate from distant lower-resolution images, typically sampling a target with 150–300 pixels. The first models generated primarily make use of limb observations. We then combine these limb-derived models with images in the SPC process to generate an initial set of low-resolution DTMs (also called maplets) or landmarks. These landmarks allow the determination of the asteroid's obliquity and rotation rate. We construct additional DTMs, produce an improved shape model, and update Bennu's obliquity and rotation rate as we obtain more images. These improvements, in turn, provide the starting model for generating additional DTMs with progressively higher GSDs, as increasingly higher-resolution imagery is available during the approach to Bennu. The collection of OCAMS data for SPC discussed in Section 2 is consist with the sequential process of continually improving the spatial resolution of the SPC-derived DTMs.

After we make the first limb models, the SPC process begins by using stereo parallax to define a relationship between surface tilts, surface brightness, and observed relative surface albedo. Sampling the asteroid with images of 300 or more pixels meets these criteria, where multiple images provide a range of observer azimuths and elevation for stereo for discrete, recognizable points across the surface of a target. This geometric stereo data defines the center pixel of the many small DTMs (maplets) spread across a target asteroid or planet. The target's spin provides vital lighting differences at any point on the surface; this makes it possible to establish the relationship between tilts and brightness within a maplet and provides an estimate of the relative albedo across the surface. The relationship between brightness and tilt is modeled using an appropriate photometric function—typically a modified Lommel-Seeliger function that was developed for the Moon (McEwen, 1996) and seems to work well for the asteroids studied to date. Testing reveals that differing photometric functions have little impact on the final products, mainly because SPC's optimum phases space is between 50 and 120°, where most photometric models behave similarly. SPC uses the photometric function, with all the imaging data available, to estimate the surface tilts at each pixel in a maplet, via a linear estimation solution that minimizes the residual of the summed square brightness at that maplet's pixel with a minimum of five and as much as a few hundred images (Fig. 9). The tilts are then integrated to heights to produce the surface shape data within each maplet, usually a 100 pixel × 100 pixel local DTM.

When building a global model, we join the individual maplets together. The mutual connections of the global model are controlled by overlapping maplets, along with the limb observations mentioned above and the global stereo parallax defining the center location of each maplet. These data constrain the tilt-to-height integration between maplets to provide the estimate of the global surface. The least squares inversion that is used to close the global model provides formal uncertainties for the spacecraft state and the shape of the target. In the end, the SPC estimation process provides solutions for an object's center of figure, pole location, wobble, rotation state, and volume (Gaskell et al., 2006, 2008; Gaskell, 2011).

As mentioned previously, extensive empirical testing indicates that, for best results, SPC requires any piece of terrain to have at least four images with four different observer elevations and azimuths, separated by a convergence angle of about 90° when in opposite E-W and N–S quadrants. The Sun angles for these images should also vary. These Sun angles need, at 45° either to the east or west. Some slight north-south Sun incidence angles are helpful when an asteroid or planet has some obliquity, to reduce shadowing effects near the pole. Also, a fifth image near 0° emission and 10° incidence is necessary to obtain good relative albedo solutions. All the images need to have comparable spatial resolution, with a minimum of one or two images at or below the desired GSD needed by the topographic model, while the other images should not exceed this GSD by more than a factor of 5.

The accuracy of an SPC shape model ultimately depends on viewing conditions. We use predicted trajectories and observation designs and assess the results following the acquisition of the observations by using reconstructed spacecraft attitudes and trajectories (e.g., Fig. 3). Further, we make estimates of the model accuracy in flight from internal SPC metrics that determine the residuals or differences in pixels between the images used to model the surface of the asteroid and the images rendered from the models produced by SPC. We also derive formal uncertainties from the least squares inversions used within SPC and the internal agreement between maplets when combined to produce the global shape model. In addition, an independent normalized cross-correlation technique is used to determine how well SPC results for the surface heights and albedo reproduce images of the surface (Palmer et al., 2018). For this correlation test, we do not include images used in the production of the SPC model. This firewall maintains independence between the evaluation undertaken and the products developed. The cross-correlation test captures the horizontal precision of the models accurately and, to a lesser degree, provides a measure of vertical precision. OLA data offers another way to evaluate SPC products, where OLA ranges to the surface can be used as a constraint to compare scale differences in images rendered from SPC DTMs and albedo with OCAMS data. Finally, a suite of "truth" model tests provides a way to predict the absolute accuracy and precision of the DTMs expected in flight, when given the viewing geometry assessments, SPC's internal metrics, and the cross-correlation results.

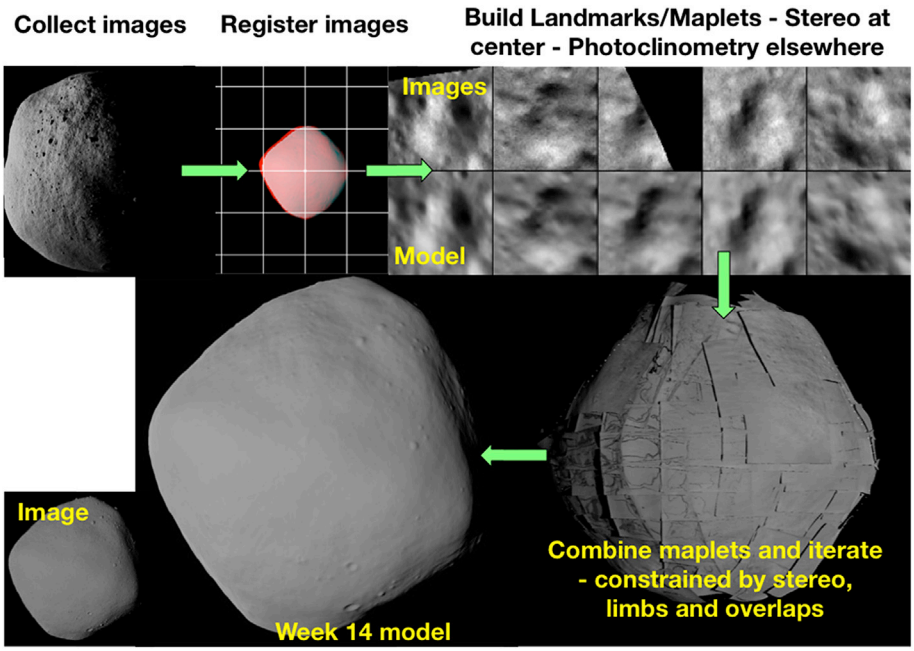

Fig. 9. Stages of the SPC process that include the initial registration of collected images to each other. This process allows construction of local DTMs or maplets, in which stereo data define the position in 3D space of the center of the maplet, and photoclinometry defines the tilts at the pixel scale of the maplet. These slopes are integrated to estimate surface heights across the maplet. The resulting individual maplets are then combined to build the overall asteroid shape, where the stereo data, the limbs, and the overlaps between maplets define the final shape model. The bottom left shows an SPC model (large) towards the end of Approach, which can be compared to an image (small) of the truth model.

3.2. Tiling OLA scans

We have two approaches for tiling the rigid OLA scan data together. The first approach uses scale-invariant feature transform (SIFT; Lowe, 1999) to find matching surface features or "keypoints" between individual OLA scans; the other uses the well-known iterative closest point algorithm (ICP; Besl and McKay, 1992). Both techniques then minimize the differences between the location of the OLA returns (a 3D "point cloud") within overlapping OLA scans to build up local and global DTMs.

The keypoint approach is our baseline method for working with OLA data (Seabrook et al., 2019). The approach begins by first filtering the OLA data for any noisy returns (Fig. 10). Then local DTMs are constructed (Fig. 4) that center on a point cloud produced with each OLA scan of the surface. The location of the point cloud in 3D space is the result of an initial estimate of the spacecraft position and pointing, the OLA scanner's pointing, and the range measured to the surface by each OLA return. For this analysis, the point cloud and its corresponding local DTM are assumed to be a rigid body, because of the demonstrated high stability of the OLA mirror (Daly et al., 2017). A Laplacian of each OLA DTM provides a 2D image showing the rate of change with distance of the surface curvature. Roberts et al. (2014) found that for asteroid 433 Eros, flat-floored depressions called "ponds" are easy to identify using such data. Inspection of their examples indicates that this Laplacian is also useful to identify matching surface features even when they are viewed on different slopes.

Consequently, the resulting Laplacian images are well-suited for use by the SIFT algorithm to identify matching keypoints and their descriptors. The SIFT algorithm was developed in the 1990s (Lowe, 1999) and is extensively used for object and facial recognition, as well as image registration. It can identify matching features over a wide range of viewing geometries and illumination. After some filtering of outliers, matched keypoints are used to compute in 3D the rigid rotation and translation needed to match overlapping OLA scans. The adjustments are made iteratively across the entire asteroid until all the differences between overlapping OLA scans are minimized. A final adjustment is then required where all the OLA scans are simultaneously transformed to minimize the differences between the new estimates of spacecraft trajectory derived from keypoint adjustment of the OLA scans and the trajectory derived by FDS. FDS estimates these trajectories using the SPC-derived landmarks but also integrates radio science results with gravity effects. The final step ensures that the center of mass of the OLA-derived shape model of Bennu is consistent with that determined by FDS.

ICP is our second approach to develop OLA-derived shape models. We use it mainly when the keypoint method fails to find matches because the OLA scans have insufficient overlap, or with unevenly spaced data. It is also beneficial for matching point clouds to existing SPC shape models to verify in flight the quality of the SPC-derived models and to further improve these models if we do not obtain a global set of overlapping OLA data. The ICP algorithm is computationally more intensive than the very rapid keypoint approach because it revises the transformation needed to minimize differences between two point clouds iteratively, using many, if not all, of the points in the point clouds. In our ICP implementation, we base the convergence criteria for matching the points on the root mean square (RMS) difference between the points in the two clouds. Because ICP uses all the points in 3D, there is no pre-processing of the OLA point cloud except removal of noisy returns. Once we remove outliers, we identify overlapping regions between OLA scans, and we use a subregion of the scan that is being transformed to match the other scan to compute the rigid translation and rotation needed to match the two scans. The identification of overlap is critical to ICP to avoid a scan transformation solution that is an incorrect local minimum and that can be difficult to identify without careful analysis. This need for careful assessment of the results of the ICP algorithm while producing a DTM, as well as high computational overhead, makes ICP much more time-consuming than the keypoint approach.

After all the OLA data are correctly strip-adjusted or corrected to each other, we build both global and local terrain models. Depending on the degree of sphericity of Bennu, one of two processes may be used to make these DTMs. In the case where Bennu is relatively spherical, the OLA data are binned globally in a latitude-longitude grid, where the grid size at the equator is half the size of the desired GSD of the shape model. When building the desired 3-million-facet shape model of Bennu, these bins are 0.30 m. The algorithm generates a global surface map by computing the median radius directly from all adjusted OLA data captured within 0.30-m grid pixels. In bins where no OLA data are present, a tension-based spline fit interpolation is used (Smith and Wessel, 2012). The gridded map is then resampled to build the Bennu 3D shape model, such that we produce facets of near-equal area across the surface. For the more general situation, where an asteroid is highly elongated (like asteroid 433 Eros)

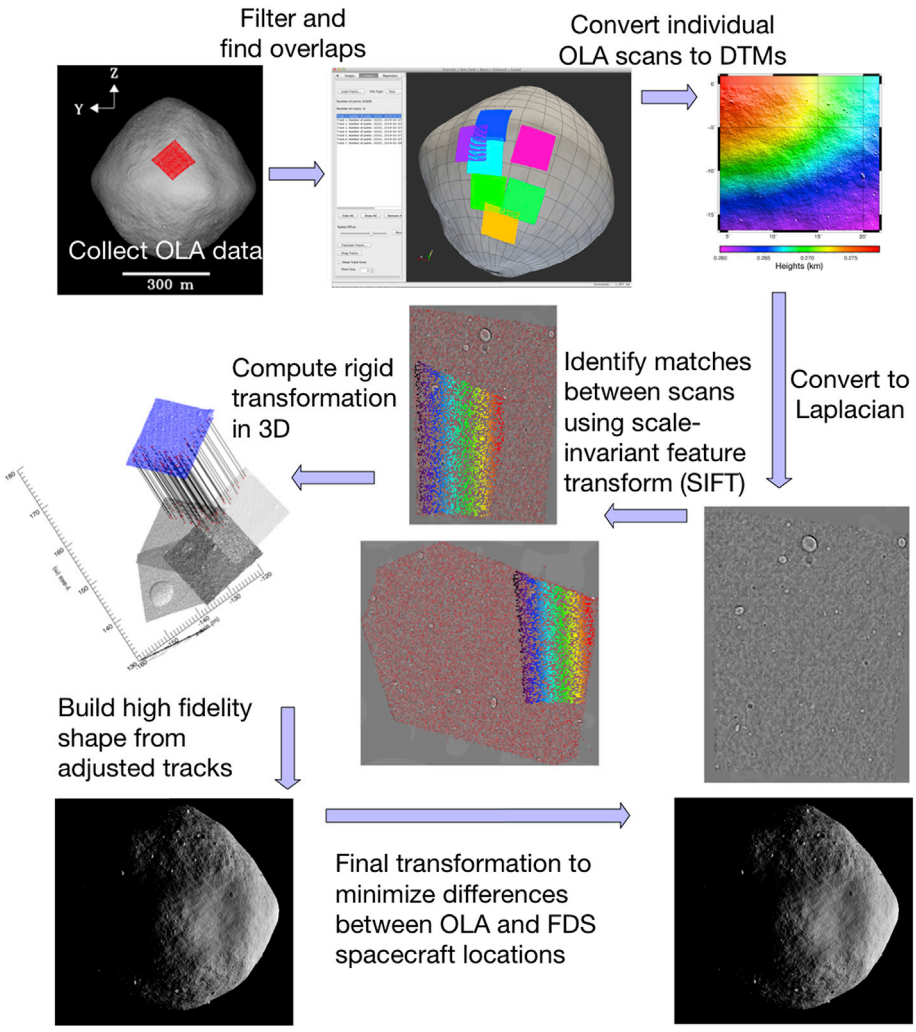

Fig. 10. OLA processing steps to make global and local DTMs using SIFT.

or has substantial concavities (like 67P/Churyumov–Gerasimenko) and or overhangs, we build a suite of small local maps ("mapolas"). The mapolas are then recombined to make the broader topographic products (asteroid shape model, global and site-specific topographic maps), using either the SPC process to combine mapolas or an alternate and equally effective method developed within the AltWG, where a smoothed global shape model is adjusted in the local normal direction to match the local mapolas.

Higher-resolution local products are produced directly by sampling the strip-adjusted OLA data in regions of interest. Suites of local OLA DTMs sampling the entire asteroid are produced at GSDs of 0.3 and 0.08 m. We produce local maps of the OSIRIS-REx sample site at GSDs of 0.05 m. Very high-resolution maps with GSDs near 0.03 m might also be possible, depending on OLA coverage.

The accuracy and precision of the OLA shape models depend on the fidelity of the strip adjustment. A key metric that we use in flight is the standard error between individual OLA points after strip adjustment. We measure this error at a given bin in a mapola. We further determine the quality of adjustment to scans by using spectral analyses where spatial differences in the frequency domain are assessed between overlapping scans after adjustment.

We also perform accuracy assessments using cross-correlation and the SIFT algorithm with images, similar to the approach used by SPC. Tests with synthetic models are used to calibrate these metrics to provide reasonable estimates of the accuracies associated with the models produced in flight.

3.3. *Combining SPC and OLA products*

We use two approaches to combine SPC products with OLA data to generate SPC-OLA products. These approaches allow cross-checks of the individual SPC and OLA products but also enable the production of final high-resolution MLNs of Bennu that include both topography from SPC and OLA and relative surface albedo from SPC. The generation of SPC-OLA products is not a critical to the success of the OSIRIS-REx mission, and a detailed description of the procedures is beyond the scope of this paper. In the two approaches, we either use OLA ranges associated with specific images taken at the same time to constrain the SPC process, or we add the previously described mapolas to the set of SPC maplets, and the SPC tools use both products to generate a final model.

4. DTM and MLN testing

We produce two sets of DTMs: (i) global shape models and DTMs and (ii) local or regional DTMs. The latter products can be tiled together to make up a global dataset, as well as providing very detailed local maps. We also generate several MLNs that include a measure of relative albedo. To verify the performance of the products that we expect to generate at Bennu, we undertook extensive testing of the SPC and OLA tiling approaches.

4.1. SPC testing

In the case of the SPC tests, we simulated images for all SPC-relevant phases of the mission, from Approach until Detailed Survey. We also simulated a subset of the images expected from Orbital B to generate and evaluate the performance of a few local MLNs with GSDs ranging from 0.08 to 0.05 m. In all cases, we included realistic spacecraft pointing uncertainties, realistic navigation errors, and the effects of uncertainties in the right ascension and declination of the pole and the rotation rate (Table 2). The simulated images were assumed to be well-calibrated, with distortion and stray light effects well understood, as would be expected in flight by the time that we begin our shape-modeling efforts.

We first generated several synthetic truth shape models of Bennu, with various states of surface roughness. A radar model of Bennu generated by Nolan et al. (2013) served as a starting point for these models. We developed the surface roughness from analyses of surface properties of 433 Eros (Cheng et al., 2002) and 25143 Itokawa (Barnouin-Jha et al., 2008) and from thermal inertia (Delbo et al., 2007; Emery et al., 2014) and radar (Nolan et al., 2013) data that indicated that Bennu would be likely to have surface properties somewhere between those of Eros and Itokawa (but see Lauretta et al., 2019; Barnouin et al., 2019 and DellaGiustina et al., 2019). To simulate a set of realistic global and regional images of the surface, we needed to construct the synthetic model to a GSD of 0.05 m globally, and 0.01 m locally for a 100 m × 100 m region where OSIRIS-REx would sample the surface. We built three of these global synthetic models, two of which became our workhorses for testing (Fig. 11).

We created the resulting test images using a NASA Goddard Space Flight Center tool called Freespace (https://software.nasa.gov/software/GSC-15480-1). For each MapCam or PolyCam pixel, a few tens to hundreds of rays were traced through the optics of the cameras, using the correct focal length for each one and simulated detector noise until they reached the surface of the simulated truth model. The images were generated using the nominal spacecraft trajectories and pointing. For the test, we delivered the images to the SPC team with perturbed spacecraft trajectories and pointing data. We produced images for all the key SPC imaging phases shown in Fig. 2.

After the first few rotation movies obtained during the simulated Approach phase, we generated a low-resolution global model from limb observations and acquired initial pole estimates. Once the spacecraft was close enough that Bennu measured over 300 pixels across, we created a set of maplets and developed the first true SPC-derived DTM model using stereo data, limb imagery, and overlaps between maplets. We then refined the pole direction and rotation. With additional data from the simulated Preliminary Survey, the model improved further, leading to a global model that satisfied the diverse navigation and scientific needs of the mission. Indeed, the data at the end of the simulated Preliminary Survey were sufficiently good to enable a switch to landmark-based navigation, where surface features rather than stars are used to determine the position of the spacecraft (Williams et al., 2018). Figs. 12 and 13 show the progression of the model relative to the truth model using the images and better-resolution data collected during the simulated Approach, Preliminary Survey, and Detailed Survey phases.

Table 2
Navigation errors associated with simulated OCAMS data used in SPC testing.

Mission Phase	RMS Differences between Nominal and Perturbed Trajectory			
	Along Track (m)	Radial (m)	Normal to Orbit Plane (m)	Delta[a] Time (s)
Approach and Preliminary Survey	60	195	5	1345
Detailed Survey: Equatorial Station	7	9	9	150

[a] Uncertainty between when observation should have been taken and when it was taken due to the trajectory errors. Affects assumed spacecraft attitude at time of observation.

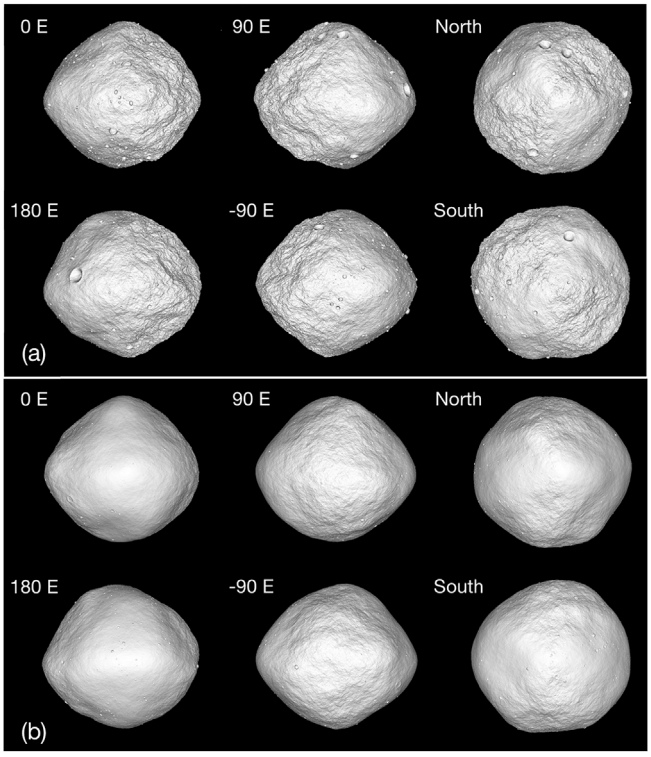

Fig. 11. Rough (a) and smooth (b) high-resolution truth models of Bennu used to test SPC and OLA processing.

The predicted quality of the final SPC products is excellent (Fig. 13). The global DTMs provide exact locations of surface features in 3D to 0.1 m RMS and tilt error uncertainties of 3.6°. The performance of these DTMs, along with SPC's solution for relative surface albedo, allows spacecraft navigators to generate digital images of the asteroid, which are suitable for direct comparisons to real images. Such comparisons allow triangulation of the location of the spacecraft relative to the asteroid. Any errors in the SPC model are due to highly tilted features such as boulders and regions not sufficiently populated with maplets (Figs. 14 and 15). Thus, SPC tends to more accurately render the shape of a surface with increasing surface smoothness (Fig. 16). Testing with alternative

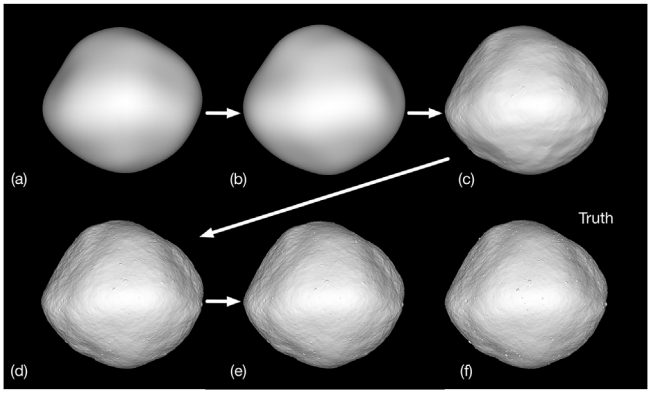

Fig. 12. Improvements in the simulated SPC shape model as a function of mission phase, beginning (a) and ending (b) in Approach, where limbs are the primary data source, followed by models produced at the beginning (c) and end (d) of the Preliminary Survey using landmarks, and the final (e) global model generated the end of Detailed Survey. The truth model is shown for comparison in (f).

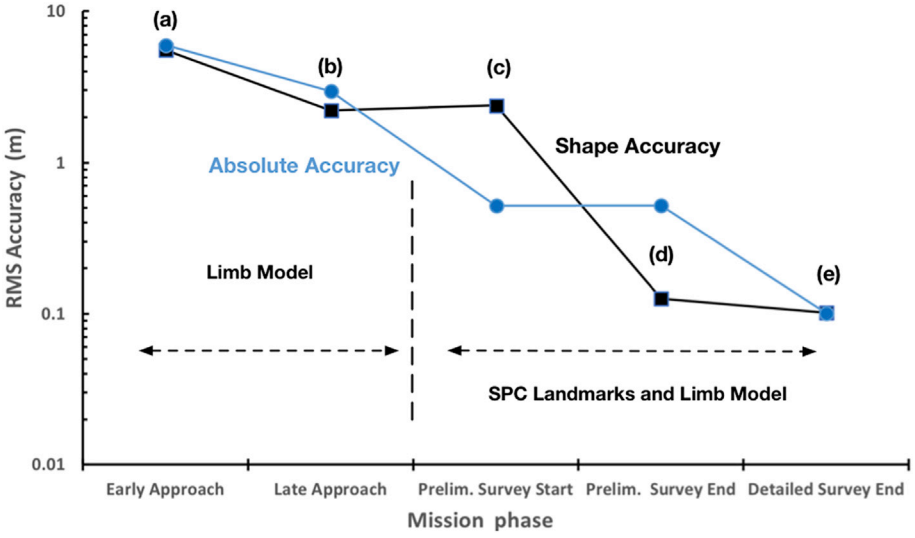

Fig. 13. Absolute (blue) and shape model (black) accuracy of global SPC models as a function of mission phase shown in Fig. 12. Absolute accuracy includes any errors in the knowledge of the center of figure relative to the center mass of the shape model used. The shape model accuracy shows how accurate the model is after any differences are minimized between a truth model and the SPC-generated shape model at the shown phase of the mission. This latter accuracy provides a measure of shape uncertainty associated with any measurement made directly from SPC-derived models. (For interpretation of the references to color in this figure legend, the reader is referred to the Web version of this article.)

photometric functions that better represent photometric properties of the asteroid does not noticeably change this finding: in SPC, there always remains some degeneracy between albedo and topography.

SPC at 67P/Churyumov–Gerasimenko and Vesta has shown that the effect of this degeneracy can be reduced using a second control for adequately modeling the surface, namely, the number of local maplets used in modeling the surface in an SPC solution. This maplet number depends on the number and resolutions of images used to generate the solution. Although there is no point-wise correlation between the error of a vertex and the number of maplets overlapping it, maps of test results show that regions with a higher number of maplets have lower RMS error

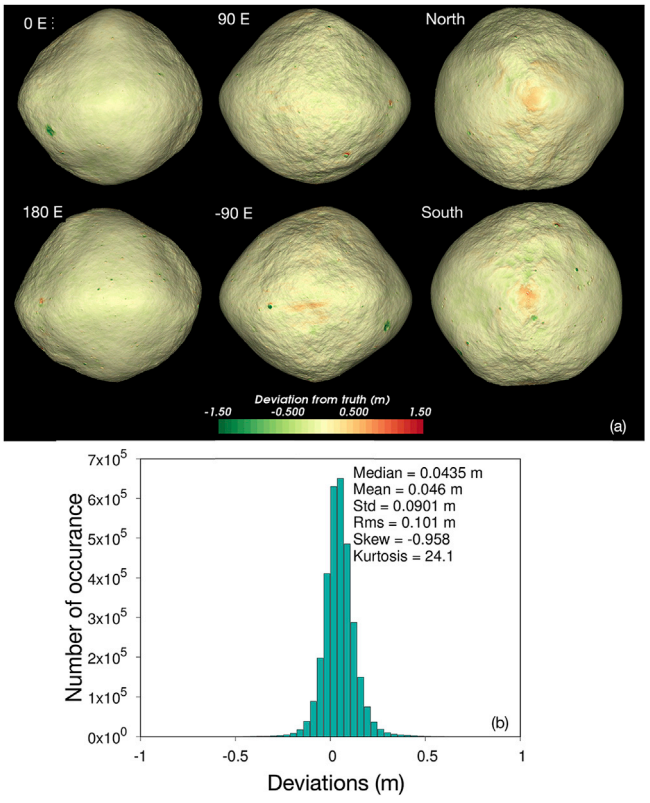

Fig. 14. Deviations in meters (a and b) between the SPC model produced at the end of the simulated Detailed Survey relative to the truth model used in the SPC test.

(Figs. 17 and 18). Additional tests in which craters and boulders were measured find that SPC effectually represents features that are 10 times the image GSD. The solution improves when at least two or three maplets sample a feature (Weirich et al., 2016). This finding is a result of the fact that SPC establishes a new stereo point at each maplet center. Accurate measurements of crater and boulders shapes on Bennu using SPC will, therefore, always take into account the total number of SPC maplets and the GSD of the input images and maplets.

4.2. OLA testing

For the OLA tests, we generated a global suite of OLA data, starting with the scans from the simulated Preliminary Survey, Detailed Survey, and Orbital B phases. We also modeled sample Recon data. For the simulated Preliminary and Detailed Surveys, we generated OLA data using a nominal planned trajectory but assumed uncertainties in the spacecraft position during the analysis. Due to the uncertainty of small-body forces influencing the spacecraft, position uncertainties are expected to dominate all other uncertainties, including pointing knowledge uncertainties. As a consequence, we did not include pointing errors in the generation of the simulated Preliminary and Detailed Survey OLA data. Table 3 lists the trajectory errors employed for Preliminary and Detailed Survey tests.

When generating the simulated Orbital B data, we used realistic orbits for observations that included sizeable down-track errors of up to 300 m. These down-track errors affect how well the spacecraft knows where "down" or nadir is two days after the navigation team updates its assessment of the spacecraft's location in its orbit. This uncertainty affects OLA planning, where optimum observations opportunities are lost just a few days after each navigation update; in worst-case scenarios, observations can be missed entirely, with the spacecraft pointing well off the asteroid. The simulated OLA data generated for this phase of the mission also include knowledge uncertainties in reconstructed pointing and position of the spacecraft. The maximum magnitude of the spacecraft position uncertainties used in the simulation is shown in Table 2 and folds in timing errors. The pointing knowledge uncertainties in the Orbital B simulations have RMS values of 0.67 mrad (3σ) for the boresight and 0.59 mrad (3σ) in roll. We then generated simulated OLA data for the Recon phase with no spacecraft errors to provide a sense of the quality of the products that we can attain in this phase of the mission.

All the synthetic OLA range data include some noise. We constructed the range measured by OLA in the simulated data using nine range estimates from OLA to the surface for each measured return. The central part of the OLA footprint contributed 50% of the range, 25% came from

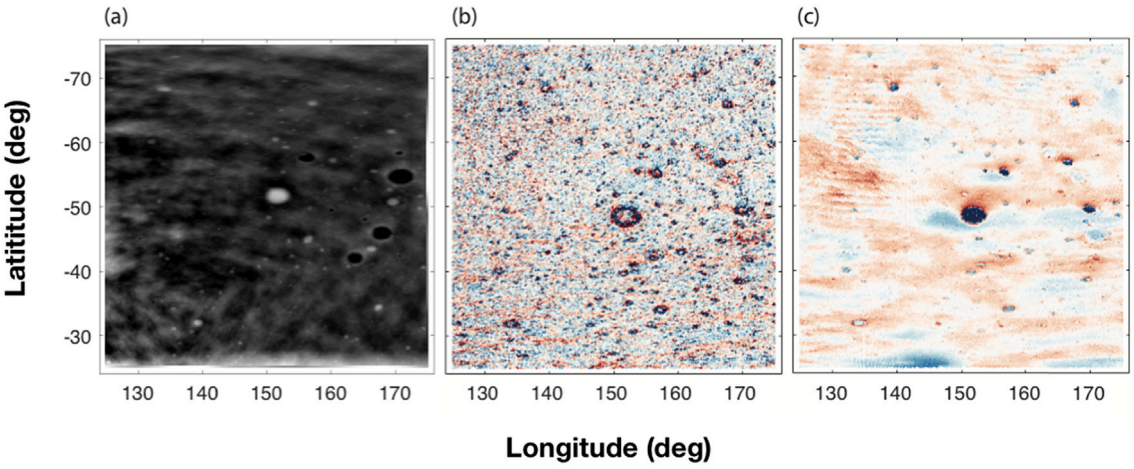

Fig. 15. Small-area study to investigate the ability of the SPC technique to represent boulders and craters. (a) High-pass filtered local 0.3-m of truth shape model where white circles represent boulders and black circles represent craters. (b) Tilt error map (truth tilt minus SPC tilt) for the same region. Blue colors are positive errors; red are negative. (c) Radial position error for the same regions. The central boulder in the area depicted shows the limitations of SPC explained in the text. The x and y axes are in degree longitude and latitude.

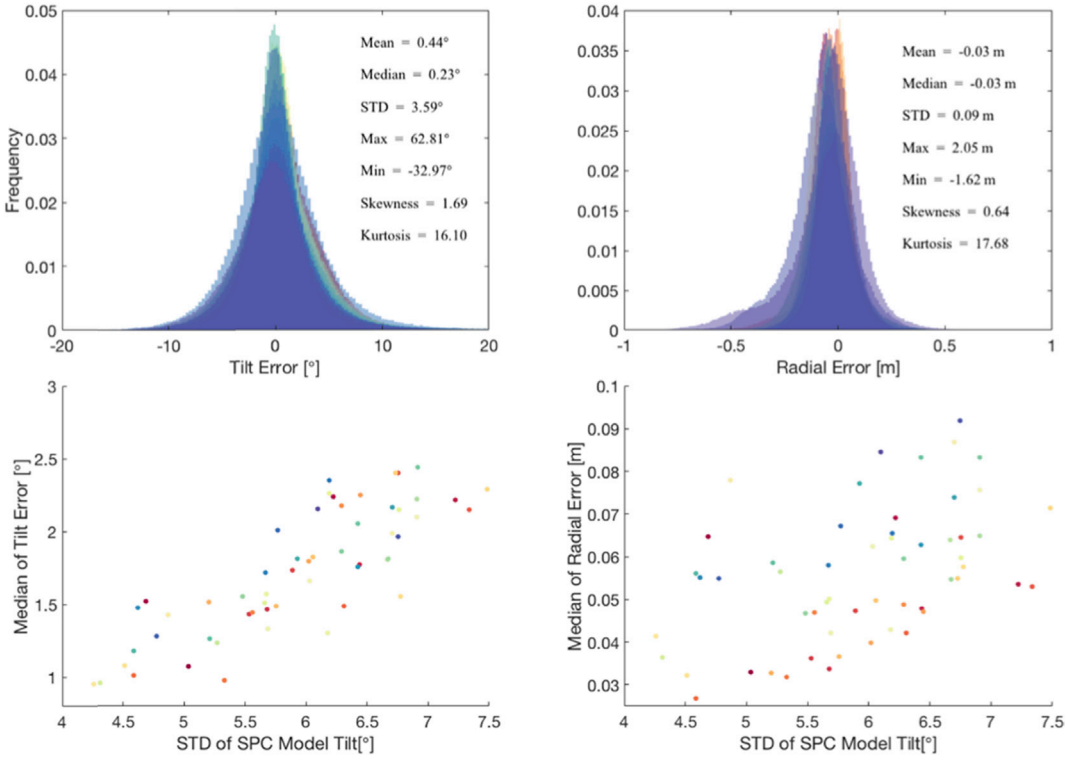

Fig. 16. Performance of SPC for all (56) 0.3-m local DTMs. In the top row, the histograms represent the error distribution for each DTM, with the statistical information provided for all DTMs combined. The bottom row plots the standard deviation of the model tilt, a measure of smoothness, with the median error in the tilt (left) and the radial position (right) for each of the DTMs.

four points equally spaced around the edge of the OLA FOV, and another 25% came from four points equally spaced around a ring at 1.4 times the OLA FOV. This approach allowed us to simulate the 1/e decay of the range pulse across an OLA footprint. We also included an additional noise term in the range of ±0.03 m (1σ). This value was the current best estimate of the performance before calibration of OLA. The laboratory verified OLA performance is ±0.01 m (1 σ; Daly et al., 2017).

The nominal OLA tile-adjustment process consists of a rough intermediate alignment followed by an iterative minimization of errors across the entire asteroid shape. Some initial test results for Detailed Survey differ from the truth model by nearly 0.21 m for the 96.6% of the surface area of the asteroid observed at emission <45˚ (Fig. 19). This value is approximately equal to the level of uncertainty associated with simulated OLA measurements obtained for the Detailed Survey stage of the mission. In a thorough assessment undertaken for Orbital B, we generated histograms of the errors as compared to the unmodified truth model (Fig. 20). The final result has a 1-sigma width of 0.054 m and is comparable to the noise injected into the test dataset. Local OLA products generated from Orbital B at GSD of 0.05 m confirm that the OLA models are within the 0.054-m (1-sigma) difference of the original synthetic truth DTMs.

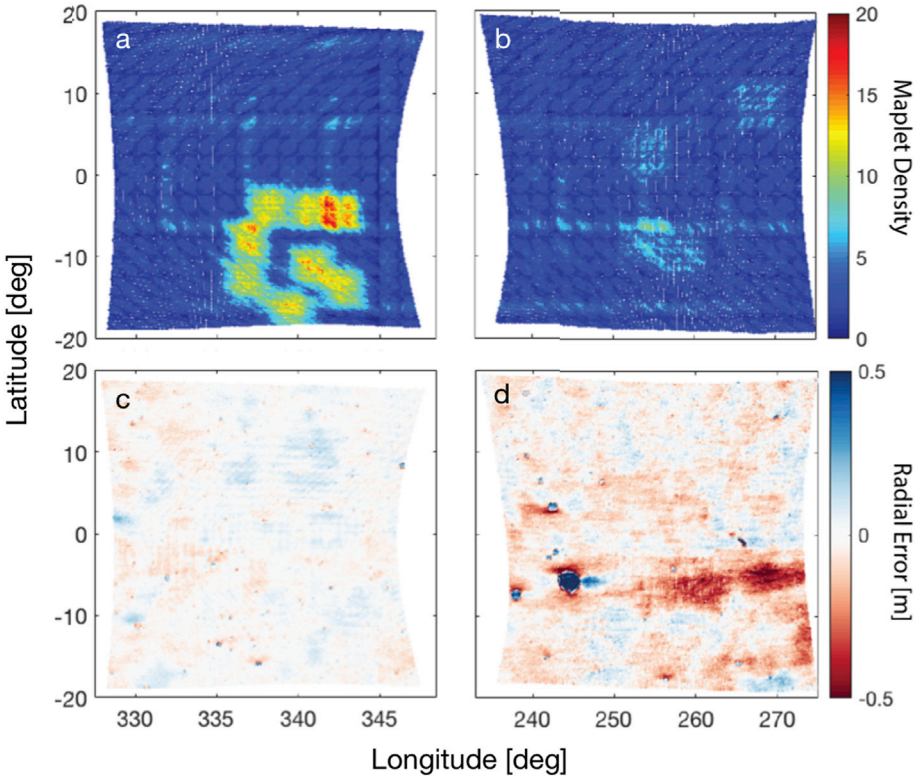

Fig. 17. Two example simulated SPC-derived DTMs (a plus c; b plus d). The left column shows a DTM that possess a higher average maplet density relative to the DTM on the right which has a lower average maplet density and higher radial error.

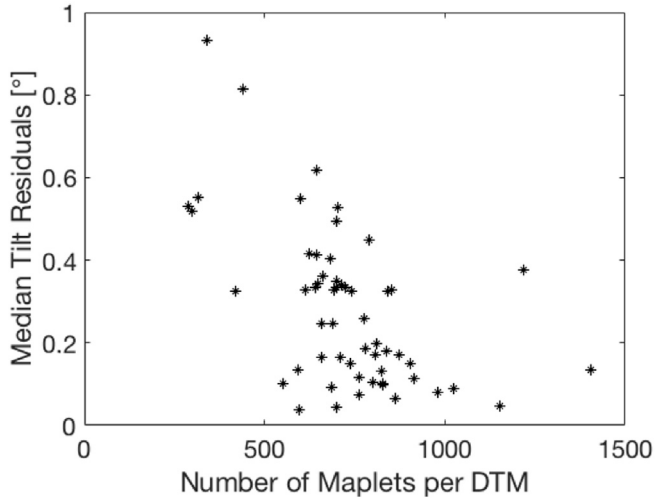

Fig. 18. The relationship between the number of maplets per local DTM and the median tilt residual for that DTM.

However, once differences are minimized with ICP between this 0.05-m OLA DTM and the truth DTM with the same GSD, we can measure the shapes of blocks and craters with precisions near ±0.015 m, which is a factor of 2 better than the noise injected into the test dataset (Fig. 21). For these OLA DTMs, a maximum of three OLA scans overlapped in most areas of the DTM, and the mean residual between the OLA returns and the DTM generated with OLA was 0.025 m. The reconstructed Recon data are even better, with a vertical precision of 0.01 m for DTMs with a GSD of 0.05 m.

Table 3
Navigation errors used to generate and tile simulated OLA data.

Mission Phase	RMS Differences between Nominal and Perturbed Trajectory used to Create Synthetic OLA data			
	Along Track (m)	Radial (m)	Normal to Orbit Plane (m)	Delta Time[a] (s)
Orbital B	≤625	≤2	≤0.5	NA
RMS Differences between Nominal and Perturbed Trajectory used to Tile OLA data				
	Along Track (m)	Radial (m)	Normal to Orbit Plane (m)	Delta Time (s)
Preliminary Survey	17	16	387	412
Detailed Survey: Equatorial Station	15	15	9	325
Orbital B	2	2	8	40

[a] Uncertainty between when observation should have been taken and when it was taken due to the trajectory errors. Affects assumed spacecraft attitude at time of observation.

5. Ancillary products

We also generate a suite of ancillary global and regional products that include SPC relative albedo, measured intensity of OLA returns, the distribution of geometric surface tilts (β), and additional measures of surface roughness. The latter two products are needed to sample the surface of the asteroid safely. We additionally use mass estimates generated by FDS and the Radio Science Working Group (Scheeres et al., 2016; McMahon et al., 2018) to provide critical geophysical products needed to constrain the provenance of the returned samples and to understand current and past surface process on Bennu. These geophysical products include estimates of surface slope, surface geopotential, the magnitude of the surface gravitational acceleration, and the geopotential altitude or elevation, where this altitude is computed like topography for

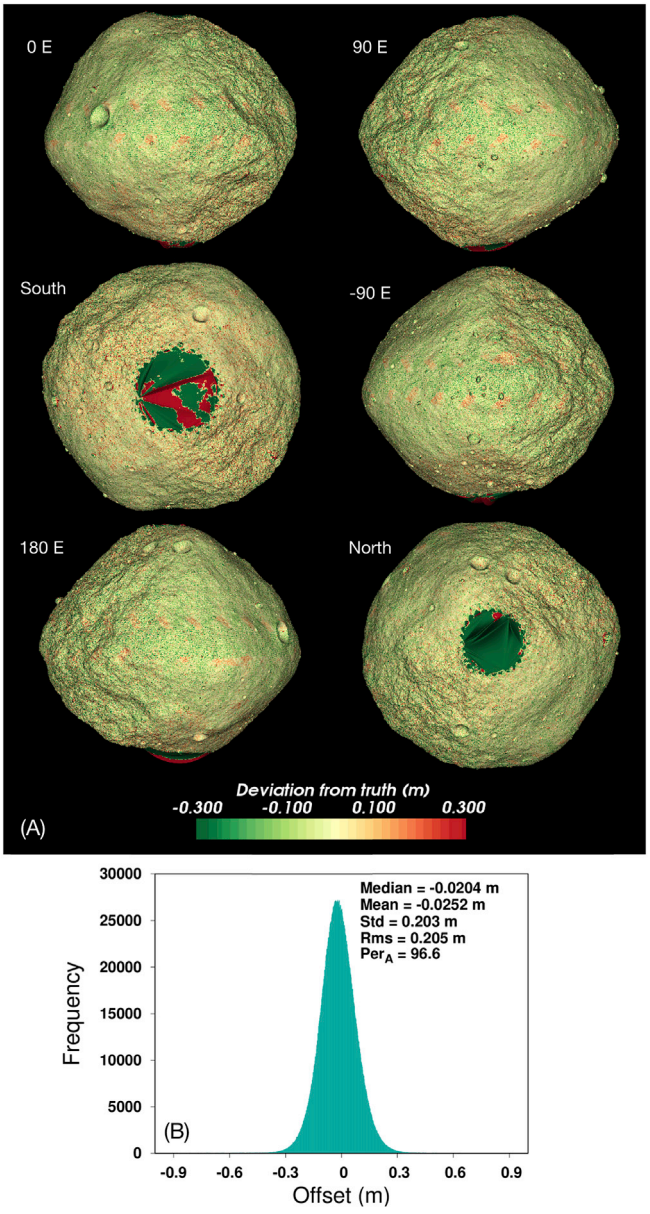

Fig. 19. Deviations in meters (a) with a histogram (b) showing differences between a model produced from synthetic OLA data collected during the simulated Detailed Survey and a truth model of Bennu. The pole areas were not included in this histogram, which covers 96.6% of the surface area of the model.

planets, relative to a geoid (Turcotte and Schubert, 1982). Table 4 lists the ancillary products, including variable definitions. The AltWG is also responsible for providing information on the volume, pole orientation, and rotation rate and defining the prime meridian and coordinate system for Bennu (see Barnouin et al., 2019).

We calculate geopotential elevation, potential, gravitational acceleration, and slope using the assumption of uniform density. We use the algorithm of Werner and Scheeres (1996) to compute the geoid and gravitational acceleration of Bennu across the asteroid's global and regional DTMs. This algorithm provides the gravitational potential U, a scalar at each facet center of the DTM shape model, and the associated surface acceleration vector $\boldsymbol{g}$. Our estimates include the effects of rotation. Once a geoid is computed, the height of the topography, e, measured at each facet center $\boldsymbol{r}$of the DTM becomes $e = [U(\boldsymbol{r}) - U_{ref}]/\ |g(\boldsymbol{r})|$ where U_{ref} is a reference potential. We expect important centrifugal effects at Bennu because of its 4.29-h rotation period (Hergenrother et al., 2013; Nolan et al., 2013). As a result, U_{ref} is set to the minimum potential computed at the surface of Bennu, rather than an areal average, as has been done for more slowly rotating asteroids such as Eros (Cheng et al., 2002) or Itokawa (Barnouin-Jha et al., 2008). Slope θ relative to $\boldsymbol{g}$ is computed using $cos\theta = \boldsymbol{r}.\boldsymbol{g}/|\boldsymbol{n}||\boldsymbol{g}|$ where $\boldsymbol{n}$ is the normal vector at each facet center $\boldsymbol{r}$.

Although these geophysical products assume uniform density, Bennu may have density heterogeneities (Scheeres et al., 2016, 2019). To quantify the consequences of this uniform density assumption on variables that are critical for assessing the geology of an asteroid—namely, the geopotential slope and elevation—we investigated the effects of reasonable internal mass distributions within Bennu, without changing the asteroid's overall mass. The density variations modeled include a low-density ridge (as an equatorial toroid), a 100–200 m spherical core, a 0.8 times scaled Bennu surrounded by a less dense regolith, and a mix of dense and less dense interior megaclasts. The magnitude of the density differences imposed varied from 250 to 1000 kg/m^3. For some of these models, the spherical harmonic terms up to degree and order four change by a few percent up to 40% relative to the uniform density case. We found that for geological interpretation, the effects of these heterogeneities on the surface slope and surface elevation do not have a substantive effect on the general trends derived when using a uniform density assumption. Compared with a constant-density model, the RMS difference in slope is 1.9° and in elevation is 5 m (or 7% of the dynamic range of the elevation), for the most extreme and plausibly least likely cases investigated, in which we introduced density heterogeneities of 1000 kg/m^3. For more reasonable assumptions, in which we introduced density heterogeneities of 250 kg/m^3, the RMS differences in slope and elevation across the surface of the asteroid were less than 1° and 1.2 m, respectively. Improved estimates of the density distribution within the asteroid, therefore, are unlikely to meaningfully alter the broad interpretations of geological surface processes acting on Bennu. The geology is more likely to provide evidence for the past rotation states of the asteroid, which may have had a much more dramatic effect on its gravitational state (Barnouin et al., 2019; Scheeres et al., 2019).

The ancillary products also address fundamental aspects of the shape and roughness of the asteroid. These are critical to finding safe sample sites on Bennu. These shape products include the magnitude and azimuth of four types of geometric surface tilt for a total of eight separate products. The tilts are similar to slope, but characterize the surface shape, and are useful for the last stages of spacecraft approach before sampling. The various tilt values computed for a global model include:

- Tilt magnitude β and direction (azimuth) α: The tilt of each facet in the DTM is relative to the radial vector $\boldsymbol{r}$ from Bennu's center to the facet center. It is computed using $cos(\beta) = \boldsymbol{n} \cdot \boldsymbol{r}/|\boldsymbol{n}||\boldsymbol{r}|$. The direction α of this tilt is determined by projecting the normal vector $\boldsymbol{n}$ into a plane that lies parallel to the pole of the asteroid, but is perpendicular to the x- and y-components of $\boldsymbol{r}$. The clocking angle in degrees of this projected vector, clockwise from north, is α.
- Average tilt β_{avg} and average tilt direction α_{avg}: The former is the average of the tilt magnitudes surrounding a given facet x, within a user-defined ellipse that surrounds this facet. The magnitude of β_{avg} is the angle between the radial vector $\boldsymbol{r}_{\mathbf{x}}$ of the central facet x and the area-weighted average normal $\boldsymbol{n}_{\mathrm{av}}$ derived from the averaging the normals for all the facets within the ellipse. The weighting by the area of each facet avoids bias due to the varying size of the facets captured inside the ellipse of interest. The clocking in degrees of the projection of $\boldsymbol{n}_{\mathrm{av}}$ onto a plane that lies parallel to the pole of the asteroid, but is perpendicular to the x and y components of R, then becomes α_{avg}.
- Relative tilt L and relative tilt direction l: The former is the tilt of a facet at a given point x relative to the local average tilt, determined over all the facets within a user-defined ellipse that surrounds the facet $\boldsymbol{r}$. We normalize the local average tilt by the area of each tilt projected into the plane defined by the average normal $\boldsymbol{n}_{\mathrm{av}}$ across all the facets within the prescribed ellipse to avoid areal biases due to the size of facets surrounding $\boldsymbol{r}$. The angle l is the direction of the facet tilt

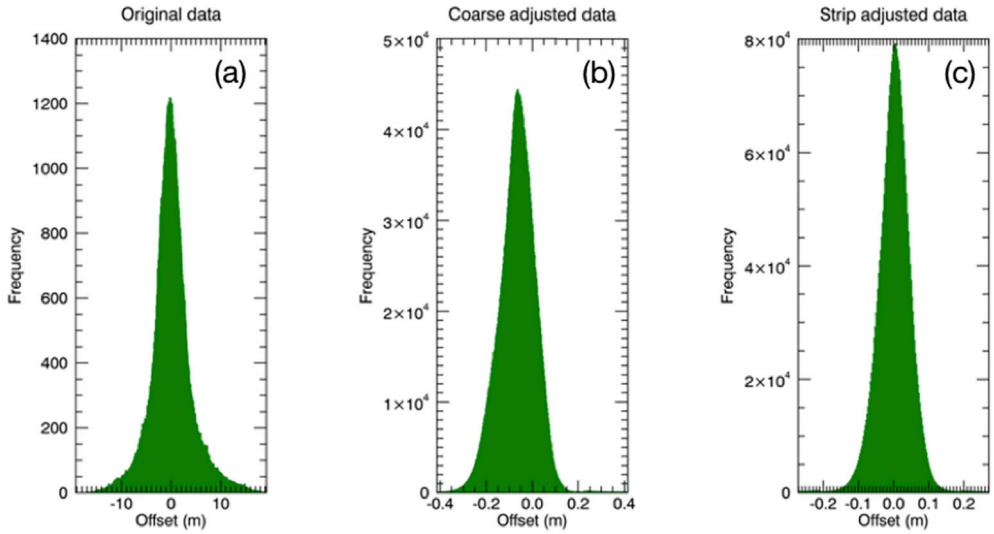

Fig. 20. Histograms of plate center to nearest intersection distance between the reference truth shape model and the simulated uncorrected OLA shape model (a; mean = 0.0468 m; σ = 3.839 m), a shape model built from the coarse adjusted shape model (b; mean = −0.0663 m; σ = 0.089 m), and the final simulated OLA strip-adjusted shape model (c; mean = −0.0016 m; σ = 0.054 m). The horizontal scales are different (see Seabrook et al., 2019 for more details).

relatve to the local average tilt and is also area-normalized. Like before, l is a clocking angle in degrees, clockwise from north.

- Tilt variation β_{std} and tilt direction variation α_{std}: The angle β_{std} is a measure of the variations of tilt across the prescribed ellipse; α_{std} provides a measure of the variations of tilt directions across a user-defined ellipse that surrounds the facet $\boldsymbol{r}$. Both are standard deviations of the tilt and tilt direction across the user-defined region of interest, and are also area-normalized. These variables provide a simple measure of surface roughness at a given baseline defined by the size of the ellipse.

In addition to these tilt estimates, we compute two other products that provide a quantification of hazards in a prescribed region of interest. In the case of RMS deviation $v(L)$, we gain insight about the surface

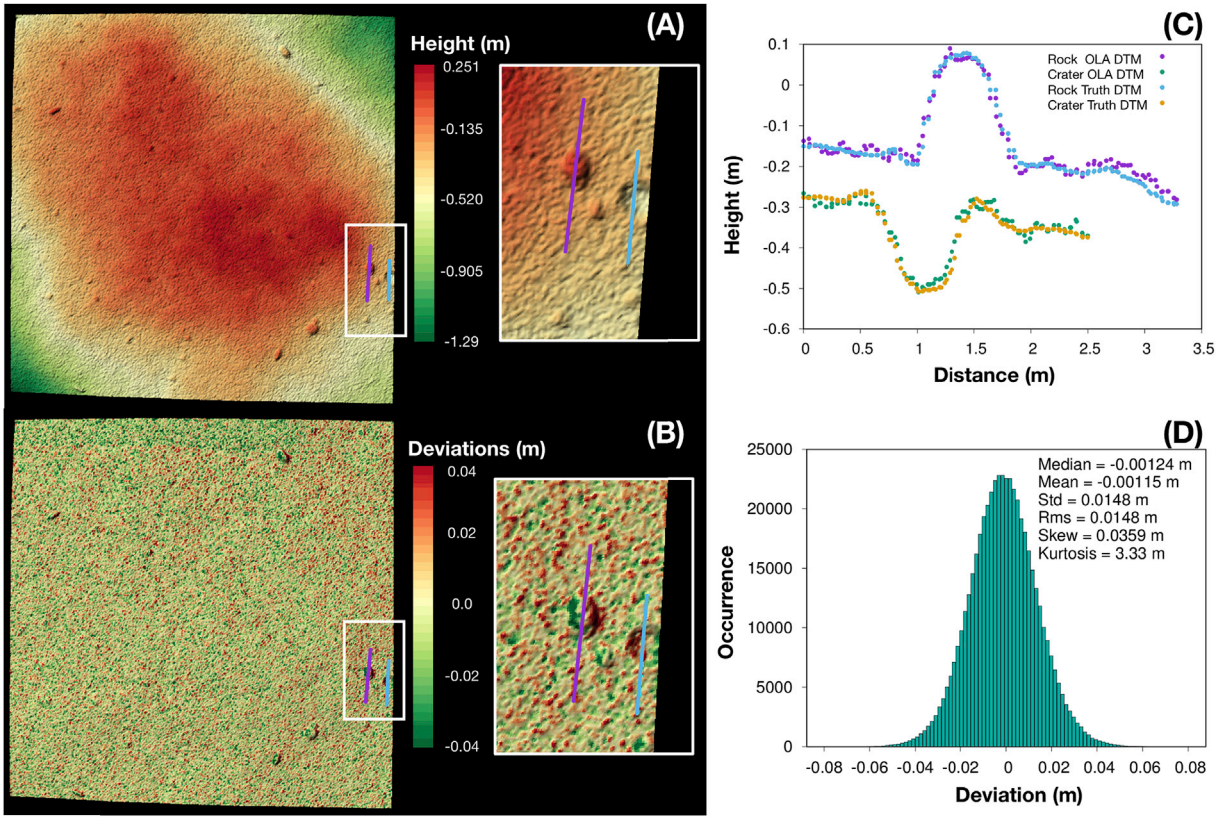

Fig. 21. Surface heights h relative to the regional plane (a) from a simulated OLA-derived DTM with a GSD of 0.05 m, produced using the rigorous Orbital B test. Deviations (b) between the OLA DTM and the synthetic truth DTM, after minimizing any differences between them, are shown statistically in the histogram (c). Resulting measurement differences between a rock and crater measured in the simulated OLA DTM and the truth DTM (d) show that we can accurately measure the shape of these 0.2-m features to within 0.01–0.02 m.

Table 4
Ancillary products.

Product	Description
SPC albedo a	Relative surface albedo, AU
OLA intensity i	Returned intensity, AU
Normal vector, $\boldsymbol{n}$	Vector normal to facet, AU
Gravity vector, $\boldsymbol{g}$	Acceleration due to gravity at each facet center, m/s^2
Gravity magnitude, g	Magnitude of $\boldsymbol{g}$, m/s^2
Potential, U	Gravitational potential, J/kg
Geopotential Elevation, e	Elevation relative to the geoid, km
Geometric height, h	Height relative a regional plane, km
Geopotential Slope, θ	Slope relative to gravity, $^\circ$
Facet tilt, β	Magnitude of the facet tilt, $^\circ$
Facet tilt direction, α	Azimuth of the facet tilt, $^\circ$
Mean tilt, β_{avg}	Average β over a prescribed region, $^\circ$
Mean tilt direction, α_{avg}	Average α over a prescribed region, $^\circ$
Tilt variation, β_{std}	Variation of β over a prescribed region, $^\circ$
Tilt direction variation, α_{std}	Variation of α over a prescribed region, $^\circ$
Relative tilt, L	Facet tilt relative to normal of a prescribed region, $^\circ$
Relative tilt direction, l	Azimuth of relative tilt, $^\circ$
Facet Radius	Radius to facet center, km
Facet area	Area of facet, km^2
Max relative height, h_{max}	Max height/depth in a prescribed region, km
RMS deviation, $\nu(L)$	An RMS height change at a given baseline distance L, m

geological processes influencing Bennu (e.g., Susorney and Barnouin, 2018):

- Maximum relative height, h_{max}: This is the magnitude of the highest or lowest point within the user-defined ellipse relative to a plane fit across all of the sample ellipse. This value is a measure of the height and depth of either the largest surface clast or crater within a region of interest. This height should be small when interacting with the surface of an object.
- The RMS deviation $\nu(L)$ is the RMS of the change in topography over a baseline (Shepard et al., 2001). It is defined as

$$\nu(L) = \left[\frac{1}{n}\sum_{i=1}^{n}\Delta h(L)_i^2\right]^{\frac{1}{2}}$$

where $h(L)$ is the change in height over a given baseline L, and n is the number of Δhs used in the calculation of RMS deviation. This value is a measure of surface roughness at the length scale of interest. For sampling by the OSIRIS-REx mission, we typically consider baselines that are smaller than the radius of the sampling ellipse and are equal to the size of the head of the sampling apparatus.

The final AltWG products are measures of relative surface albedo. Generated by SPC, these are produced concurrently with the topography solution. The relative albedo estimate, which is directly related to geometric albedo, but does not have the same units, provides a notional idea of bright and dark areas across the asteroid and permits the reasonable rendering of a surface when the SPC DTM and albedo are combined. True albedo products are being generated separately by the OSIRIS-REx Image Processing Working Group (DellaGiustina et al., 2018).

Similarly, the OLA instrument provides a measure of the intensity of the surface at 1064 nm. This measurement combines reflectance and the surface roughness within an individual OLA footprint. The initial data product from this measurement is not calibrated but highlights bright and rough areas at the scale of the OLA FOV across the surface of the asteroid. At later stages in the mission, attempts will be made to disentangle surface roughness effects from reflectance and provide a measure of both from the OLA data.

6. Conclusions

We provide an overview of the methods used by the Altimetry Working Group of the OSIRIS-REx mission to produce DTM products of asteroid Bennu. These include global shape models of Bennu inferred from camera-based stereophotoclinometry and lidar-based laser altimetry. These two independently derived types of products allow direct comparisons of models. Tests show that products of very high quality can be produced from the OSIRIS-REx observations, approaching centimeter scales at the time when OSIRIS-REx samples Bennu. We also describe the full set of ancillary products based on the DTMs. The products discussed here support scientific assessments and decisions about spacecraft operations and safety.

Acknowledgments

This material is based upon work supported by NASA under Contracts NNM10AA11C, NNG12FD66C, and NNG13FC02C issued through the New Frontiers Program. We also acknowledge the funding of the Canadian Space Agency to the Canadian authors of this manuscript. We also grateful acknowledge reviews from one anonymous reviewer and Dr. Alexander Stark (DLR). We thank the entire OSIRIS-REx team for making the encounter with Bennu possible.

Appendix A. Supplementary data

Supplementary data to this article can be found online at https://doi.org/10.1016/j.pss.2019.104764.

References

Barnouin, O.S., Daly, M.G., Palmer, E.E., Gaskell, R.W., Weirich, J.R., Johnson, C.L., Al Asad, M.M., Roberts, J.H., Perry, M.E., Susorney, H.C.M., Daly, R.T., Bierhaus, E.B., Seabrook, J.A., Espiritu, R.C., Nair, A.H., Nguyen, L., Neumann, G.A., Ernst, C.M., Boynton, W.V., Nolan, M.C., Adam, C.D., Moreau, M.C., Rizk, B., Drouet D'Aubigny, C.Y., Jawin, E.R., Walsh, K.J., Michel, P., Schwartz, S.R., Ballouz, R.-L., Mazarico, E.M., Scheeres, D.J., McMahon, J.W., Bottke, W.F., Sugita, S., Hirata, N., Hirata, N., Watanabe, S.-i., Burke, K.N., DellaGiustina, D.N., Bennett, C.A., Lauretta, D.S., The OSIRIS-REx Team, 2019. Shape of (101955) Bennu indicative of a rubble pile with internal stiffness. Nat. Geosci. 12 (4), 247–252.

DellaGiustina, D.N., Emery, J.P., Golish, D.R., Rozitis, B., Bennett, C.A., Burke, K.N., Ballouz, R.-L., Becker, K.J., Christensen, P.R., Drouet d'Aubigny, C.Y., Hamilton, V.E., Reuter, D.C., Rizk, B., Simon, A.A., Asphaug, E., Bandfield, J.L., Barnouin, O.S., Barucci, M.A., Bierhaus, E.B., Binzel, R.P., Bottke, W.F., Bowles, N.E., Campins, H., Clark, B.C., Clark, B.E., Connolly Jr, H.C., Daly, M.G., de Leon, J., Delbo, M., Deshapriya, J.D.P., Elder, C.M., Fornasier, S., Hergenrother, C.W., Howell, E.S., Jawin, E.R., Kaplan, H.H., Kareta, T.R., Le Corre, L., Li, J.-Y., Licandro, J., Lim, L.F., Michel, P., Molaro, J., Nolan, M.C., Pajola, M., Popescu, M., Rizos Garcia, J.L., Ryan, A., Schwartz, S.R., Shultz, N., Siegler, M.A., Smith1, P.H., Tatsumi, E., Thomas, C.A., Walsh, K.J., Wolner, C.W.V., Zou, X.-D., Lauretta, D.S., The OSIRIS-REx Team, 2019. Properties of rubble-pile asteroid (101955) Bennu from OSIRIS-REx imaging and thermal analysis. Nat. Astron. 1–11.

Abe, S., Mukai, T., Hirata, N., Barnouin-Jha, O.S., Cheng, A.F., Demura, H., Gaskell, R.W., Hashimoto, T., Hiraoka, K., Honda, T., Kubota, T., Matsuoka, M., Mizuno, T., Nakamura, R., Scheeres, D.J., 2006. Mass and local topography measurements of Itokawa by Hayabusa. M Science 312 (5778), 1344–1347.

Barnouin-Jha, Olivier, S., Cheng, Andrew F., Mukai, Tadashi, Abe, Shinsuke, Hirata, Naru, Nakamura, Ryosuke, Gaskell, Robert W., Saito, Jun, Clark, Beth E., 2008. Small-scale topography of 25143 Itokawa from the Hayabusa laser altimeter. Icarus 198 (1), 108–124.

Besl, Paul J., McKay, Neil D., 1992. Method for registration of 3-D shapes. In: Proceedings Of the Spie, 586–606. General Motors Research Labs. International Society for Optics, USA (Photonics).

Besse, S., Kuppers, M., Barnouin, O.S., Thomas, N., Benkhoff, J., 2014. "Lutetia's lineaments. Planet. Space Sci. August, 1–10.

Bierhaus, E.B., Clark, B.C., Harris, J.W., Payne, K.S., Dubisher, R.D., Wurts, D.W., et al., 2018. The OSIRIS-rex spacecraft and the touch-and-go sample acquisition mechanism (TAGSAM). Space Sci. Rev. 214 (7), 107.

Bos, B.J., Ravine, M.A., Caplinger, M., Schaffner, J.A., Ladewig, J.V., Olds, R.D., Norman, C.D., et al., 2018. Touch and go camera system (TAGCAMS) for the OSIRIS-rex asteroid sample return mission. Space Sci. Rev. 214 (1), 37.

Bottke, William F., Vokrouhlický, David, Walsh, Kevin J., Delbo, Marco, Michel, Patrick, Lauretta, Dante S., Campins, Humberto, Harold, C., Connolly, Jr, Scheeres, Daniel J., Chelsey, Steven R., 2015. In search of the source of asteroid (101955) Bennu: applications of the stochastic YORP model. Icarus 247, 191–217.

Buczkowski, Debra L., Barnouin, Olivier S., Prockter, Louise M., 2008. 433 Eros lineaments: global mapping and analysis. Icarus 193, 39–52.

Campins, H., Alessandro, Morbidelli, Tsiganis, K., De León, J., Licandro, J., Lauretta, D., 2010. The origin of Asteroid 101955 (1999 RQ36). Astrophys. J. Lett. 721 (1), L53.

Cheng, Andrew F., Barnouin-Jha, Olivier, Zuber, Maria T., Joseph, Veverka, Smith, David E., Neumann, Gregory A., Robinson, Mark, et al., 2001. Laser altimetry of small-scale features on 433 Eros from NEAR-shoemaker. Science 292 (5), 488–491.

Cheng, A.F., Barnouin-Jha, O.S., Prockter, L., Zuber, M.T., Neumann, G., Smith, D.E., Garvin, J., Robinson, M., Veverka, J., Thomas, P.C., 2002. Small-scale topography of 433 Eros from laser altimetry and imaging. Icarus 155, 51–74.
Chesley, Steven R., Farnocchia, Davide, Nolan, Michael C., Vokrouhlický, David, Chodas, Paul W., Milani, Andrea, Federica, Spoto, et al., 2014. Orbit and bulk density of the OSIRIS-REx target Asteroid (101955) Bennu. Icarus 235, 5–22.
Daly, M.G., S Barnouin, O., Dickinson, C., Seabrook, J., Johnson, C.L., Cunningham, G., Haltigin, T., et al., 2017. The OSIRIS-rex laser altimeter (OLA) investigation and instrument. Space Sci. Rev. 198 (1), 1–26.
Delbo, Marco, dell'Oro, Aldo, Harris, Alan W., Mottola, Stefano, Mueller, Michael, 2007. Thermal inertia of near-Earth asteroids and implications for the magnitude of the Yarkovsky effect. Icarus 190, 236–249.
DellaGiustina, D.N., Bennett, C.A., Becker, K., R Golish, D., Le Corre, L., Cook, D.A., Edmundson, K.L., Chojnacki, M., Sutton, S.S., Milazzo, M.P., Carcich, B., Nolan, M.C., Habib, N., Burke, K.N., Becker, T., Smith, P.H., Walsh, K.J., Getzandanner, K., Wibben, D.R., Leonard, J.M., Westermann, M.M., Polit, A.T., Kidd Jr, J.N., Hergenrother, C.W., Boynton, W.V., Backer, J., Sides, S., Mapel, J., Berry, K., Roper, H., Drouet d'Aubigny, C., Rizk, B., Crombie, M.K., Kinney-Spano, E.K., de León, J., Rizos, J.L., Licandro, J., Campins, H.C., Clark, B.E., Enos, H.L., Lauretta, D.S., 2018. Overcoming the challenges associated with image-based mapping of small bodies in preparation for the OSIRIS-rex mission to (101955) Bennu. Earth Space Sci. 5 (12), 929–949.
Emery, J.P., Fernández, Y.R., Kelley, M.S.P., nèe Crane, K T Warden, Hergenrother, C., Lauretta, D.S., Drake, M.J., Campins, H., Ziffer, J., 2014. Thermal infrared observations and thermophysical characterization of OSIRIS-REx target asteroid (101955) Bennu. Icarus 234, 17–15.
Gaskell, Robert W., 2011. Optical navigation near small bodies. Proc. 21st AAS/AIAA Space Flight Mechancis Meet. 140 (11–220), 13.
Gaskell, R.W., Synnott, S.P., McEwen, A.S., Schaber, G.G., 1988. Large-scale topography of Io - implications for internal structure and heat transfer. Geophys. Res. Lett. 15 (6), 581–584.
Gaskell, R.W., Barnouin-Jha, O.S., Scheeres, D.J., Mukai, T., Hirata, N., Abe, S., Saito, J., et al., 2006. Landmark navigation studies and target characterization in the Hayabusa encounter with Itokawa.. In: AIAA/Aas Astrodynamics Specialist Conference and Exhibit. American Institute of Aeronautics, Reston, Virigina (Astronautics).
Gaskell, R.W., Barnouin-Jha, O.S., Scheeres, D.J., Konopliv, A.S., Mukai, T., Abe, S., Saito, J., et al., 2008. Characterizing and navigating small bodies with imaging data. Meteorit. Planet. Sci. 43 (6), 1049–1061.
Hergenrother, Carl W., Nolan, Michael C., Binzel, Richard P., Cloutis, Edward A., Barucci, Maria Antonietta, Michel, Patrick, Scheeres, Daniel J., et al., 2013. Lightcurve, color and phase function photometry of the OSIRIS-REx target asteroid (101955) Bennu. Icarus 226 (1), 663–670.
Jackman, Coralie, D., Nelson, Derek S., McCarthy, Leilah K., Finley, Tiffany J., Liounis, Andrew J., Getzandanner, Kenneth M., Antreasian, Peter G., Moreau, Michael C., 2017. Optical navigation concept of operations for the osiris-rex mission. In: Advances In the Astronautical Sciences. KinetX, Inc., United States, 3337–54.
Jaumann, R., Williams, D.A., Buczkowski, D.L., Yingst, R.A., Preusker, F., Hiesinger, H., Schmedemann, N., et al., 2012. "Vesta's shape and morphology. Science 336 (6), 687.
Lauretta, D.S., Bartels, A.E., Barucci, M.A., Bierhaus, E.B., Binzel, R.P., Bottke, W.F., Campins, H., et al., 2015. The OSIRIS-REx target asteroid (101955) Bennu: constraints on its physical, geological, and dynamical nature from astronomical observations. Meteorit. Planet. Sci. 50 (4), 834–849.
Lauretta, D.S., Balram-Knutson, S.S., Beshore, E., Boynton, W.V., Drouet D'Aubigny, C., DellaGiustina, D.N., Enos, H.L., et al., 2017. OSIRIS-REx: sample return from asteroid (101955) Bennu. Space Sci. Rev. 71 (1), 1–60.
Lauretta, D.S., DellaGiustina, D.N., Bennett, C.A., Golish, D.R., Becker, K.J., Balram-Knutson, S.S., Barnouin, O.S., Becker, T.L., Bottke, W.F., Boynton, W.V., Campins, H., Clark, B.E., Connolly Jr, H.C., Drouet d'Aubigny, C.Y., Dworkin, J.P., Emery, J.P., Enos, H.L., Hamilton, V.E., Hergenrother, C.W., Howell, E.S., Izawa, M.R.M., Kaplan, H.H., Nolan, M.C., Rizk, B., Roper, H.L., Scheeres, D.J., Smith, P.H., Walsh, K.J., Wolner, C.W.V., the OSIrIS-rex team, 2019. The unexpected surface of asteroid (101955) Bennu. Nature 1–16.
Lowe, D.G., 1999. Object recognition from local scale-invariant features. In: Proceedings Of the Seventh Ieee International Conference On Computer Vision, vol. 2. IEEE, 1150–7.
Marchi, S., Chapman, C.R., Barnouin, O.S., Richardson, J.E., Vincent, J.-B., 2015. Cratering on asteroids. In: Asteroids Iv. University of Arizona Press, pp. 725–744.
Mario, Courtney, Debrunner, Chris, 2016. Robustness and performance impacts of optical-based feature tracking to Osiris-rex asteroid sample collection mission. In: Advances in the Astronautical Sciences. Charles Stark Draper Lab Inc, Cambridge, United States, 513–23.
McEwen, A.S., 1996. A precise lunar photometric function. Lunar Planet. Sci. 27 (March).
McMahon, J.W., Scheeres, D.J., Hesar, S.G., Farnocchia, D., Chesley, S., Lauretta, D., 2018. The OSIRIS-REx radio science experiment at Bennu. Space Sci. Rev. 214 (1), 43.
Miyamoto, Hideaki, Yano, Hajime, Scheeres, Daniel J., Abe, Shinsuke, Barnouin-Jha, Olivier, Cheng, Andrew F., Demura, Hirohide, et al., 2007. Regolith migration and sorting on asteroid Itokawa. Science 316 (5), 1011.
Murdoch, N., Sánchez, P., Schwartz, S.R., Miyamoto, H., 2015. Asteroid surface geophysics. In: Asteroids Iv. University of Arizona Press, pp. 767–792.
Nolan, Michael C., Magri, Christopher, Ellen S Howell, Lance A M Benner, Giorgini, Jon D., Hergenrother, Carl W., Scott Hudson, R., et al., 2013. Shape model and surface properties of the OSIRIS-REx target Asteroid (101955) Bennu from radar and lightcurve observations. Icarus 226, 629–640.
Palmer, E.E., Weirich, J.R., Campbell, T., Barnouin, O.S., Daly, M.G., Lauretta, D.S., 2018. Image cross correlation as a measurement of shape model quality. LPSC 49, 1106 (Abstract).
Rizk, B., Drouet d'Aubigny, C., Golish, D., Fellows, C., Merrill, C., Smith, P., Walker, M.S., et al., 2018. OCAMS: the OSIRIS-rex camera suite. Space Sci. Rev. 214 (1), 26.
Roberts, James H., Kahn, Eliezer G., Barnouin, Olivier S., Ernst, Carolyn M., Prockter, Louise M., Gaskell, Robert W., 2014. Origin and flatness of ponds on asteroid 433 Eros. Meteorit. Planet. Sci. 49 (10), 1735–1748.
Rubincam, David Parry, 2000. Radiative spin-up and spin-down of small asteroids. Icarus 148 (1), 2–11.
Scheeres, D.J., Hesar, S.G., Tardivel, S., Hirabayashi, M., Farnocchia, D., McMahon, J.W., Chesley, S.R., et al., 2016. The geophysical environment of Bennu. Icarus 276 (September), 116–140.
Scheeres, D., McMahon, J.W., French, A.S., Brack, D.N., Chesley, S.R., Farnocchia, D., Takahashi, Y., Leonard, J.M., Geeraert, J., Page, B., Antreasian, P., Getzandanner, K., Rowlands, D., Mazarico, E.M., Small, J., Highsmith, D.E., Moreau, M., Emery, J.P., Rozitis, B., Hirabayashi, M., Sánchez, P., Van wal, S., Tricarico, P., Ballouz, R.-L., Johnson, C.L., Al Asad, M.M., Susorney, H.C.M., Barnouin, O.S., Daly, M.G., Seabrook, J.A., Gaskell, R.W., Palmer, E.E., Weirich, J.R., Walsh, K.J., Jawin, E.R., Bierhaus, E.B., Michel, P., Bottke, W.F., Nolan, M.C., Connolly Jr, H.C., Lauretta, D.S., The OSIRIS-REx Team, 2019. The dynamic geophysical environment of (101955) Bennu based on OSIRIS-REx measurements. Nat. Astron. 3 (4), 352–361.
Seabrook, J.A., Daly, M.G., Barnouin, O.S., Johnson, C.L., Nair, A.H., Bierhaus, E.B., Boynton, W., Espiritu, R.C., Gaskell, R.W., Palmer, E., Nguyen, L., Nolan, M., Lauretta, D.S., 2019. Global shape modeling using the OSIRIS-rex scanning laser altimeter. Planet. Space Sci. https://doi.org/10.1016/j.pss.2019.07.003.
Shepard, Michael K., Campbell, Bruce A., Bulmer, Mark H., Farr, Tom G., Gaddis, Lisa R., Plaut, Jeffrey J., 2001. The roughness of natural terrain: a planetary and remote sensing perspective. J. Geophys. Res.: Solid Earth (19782012) 106 (E12), 32777–32795.
Smith, W.H.F., Wessel, P., 2012. Gridding with Continuous Curvature Splines in Tension. " *Geophysics* (February).
Susorney, Hannah C.M., Barnouin, Olivier S., 2018. The global surface roughness of 433 Eros from the NEAR laser rangefinder. Icarus 314, 299–310.
Thomas, P.C., Robinson, Mark S., 2005. Seismic resurfacing by a single impact on the asteroid 433 Eros. Nature 436, 366–369.
Tonge, Andrew L., Ramesh, K.T., Olivier, Barnouin, 2016. A model for impact-induced lineament formation and porosity growth on Eros. Icarus 266 (March), 76–87.
Turcotte, Donald L., Schubert, Gerald, 1982. Geodynamics: Application of Continuum Physics to Geological Problems. Cambridge University Press.
Walsh, Kevin J., Marco, Delbó, Bottke, William F., Vokrouhlický, David, Lauretta, Dante S., 2013. Introducing the Eulalia and new Polana asteroid families: Re-assessing primitive asteroid families in the inner Main Belt. Icarus 225 (1), 283–297.
Walsh, Kevin J., Richardson, Derek C., Michel, Patrick, 2008. Rotational breakup as the origin of small binary asteroids. Nature 454 (7), 188–191.
Weirich, J.R., Palmer, E.E., Gaskell, R.W., 2016. Testing of stereophotoclinometry (SPC) software in support of the OSIRIS-rex mission. 47th Lunar Planet. Sci. Conf. 47, 2777.
Werner, Robert A., Scheeres, Daniel J., 1996. Exterior gravitation of a polyhedron derived and compared with harmonic and mascon gravitation representations of asteroid 4769 Castalia. Celest. Mech. Dyn. Astron. 65 (September), 313.
Wilkison, Sarah L., Robinson, Mark S., Thomas, Peter C., Veverka, Joseph, McCoy, Timothy J., Murchie, Scott L., Prockter, Louise M., Yeomans, Donald K., 2002. An estimate of eros's porosity and implications for internal structure. Icarus 155, 94–103.
Williams, B., Antreasian, P., Carranza, E., Jackman, C., Leonard, J., Nelson, D., Page, B., et al., 2018. OSIRIS-REx flight dynamics and navigation design. Space Sci. Rev. 214 (4), 69.
Wolf, P.R., Dewitt, A.B., 2000. Elements of Photogrammetry, with Application in Gis, third ed. Mcgraw Hill, Boston: McGraw Hill.
Yeomans, D.K., Barriot, J.P., Dunham, D.W., Farquhar, R.W., Giorgini, J.D., Helfrich, C.E., Konopliv, A.S., et al., 1997. Estimating the mass of asteroid 253 mathilde from tracking data during the NEAR flyby. Science 278 (5346), 2106–2109.
Yeomans, D.K., Antreasian, P.G., Cheng, A., Dunham, D.W., Farquhar, R.W., Gaskell, R.W., Giorgini, J.D., et al., 1999. Estimating the mass of asteroid 433 Eros during NEAR spacecraft flyby. Science 285 (5427), 560–561.
Yu, Yang, Richardson, Derek C., Michel, Patrick, Schwartz, Stephen R., Ronald-Louis, Ballouz, 2014. Numerical predictions of surface effects during the 2029 close approach of Asteroid 99942 Apophis. Icarus 242 (C), 82–96.